Task 1.2

Title

Reservoir stimulation and engineering

Projects (presented on the following pages)

Tracer based characterization of the connected fracture volume in the DUG Lab at the Grimsel Test Site
Alternative: Work Package 5
A. Kittilä, K. Evans, M. Jalali, M. Willmann, M. O. Saar

In situ characterization of groundwater flow and heat transport in stimulated fractured network using DTS
M. Klepikova, B. Brixel, M. Jalali, S. Loew, F. Amann

How much can we interpret mineral surface area with distributions of minerals and pores?
X. Kong, J. Ma, D. Webster, M. O. Saar

Geological characterization and in-situ stress state of the ISC experimental volume
Alternative: Work Package 5
H. Krietsch, V. Gischig, F. Amann, J. Doetsch, M. Jalali, B. Valley

Deformation and tilt measurements during the ISC experiment at the Grimsel Test Site
Alternative: Work Package 5
H. Krietsch, V. Gischig, B. Valley, F. Amann

Core-scale reactive transport modelling of injection of CO_2-charged brine into natural sandstone
J. Ma, X. Kong, M. O. Saar

Mixed finite element method for recovering stress and displacement fields
M. Nejati, T. Driesner

Numerical Modeling of Natural Convection in Fractured Media
J. Patterson, T. Driesner

Enhancing drilling performance by combining conventional and thermal spallation drilling: A feasibility study
E. Rossi, M. A. Kant, C. Madonna, M. O. Saar, P. R. von Rohr

Pico-seismicity during hydraulic stimulation experiments at the Grimsel Test Site
Alternative: Work Package 5
L. Villiger, V. Gischig, J. Doetsch, H. Krietsch, M. Jalali, N. Dutler, B. Valley, K. Evans, F. Amann, S. Wiemer

An Implicit Level Set Scheme to simulate planar 3D hydraulic fracture propagation
H. Zia, B. Lecampion

SCCER SoE
SWISS COMPETENCE CENTER for ENERGY RESEARCH
SUPPLY of ELECTRICITY

SCCER-SoE Annual Conference 2017

In cooperation with the CTI
Energy
Swiss Competence Centers for Energy Research
Schweizerische Eidgenossenschaft
Confédération suisse
Confederazione Svizzera
Confederaziun svizra
Swiss Confederation
Commission for Technology and Innovation CTI

Scaling spatial distribution of fractures using borehole images: An application to Basel geothermal reservoir

Mohammad J. Afshari(1), Benoît Valley(2), and Keith Evans(3)
(1) ETH Zürich, Geological Institute (mohammad.moein@erdw.ethz.ch)
(2) University of Neuchâtel, Center for Hydrogeology and Geothermics
(3) ETH Zürich, Institute of Geophysics

Motivation

Characterization of the natural fractures is key to create a geological model which permits the accurate design and assessment of Enhanced Geothermal System (EGS) development strategies. Our knowledge about the existing fractures in early stages of reservoir creation is restricted to borehole data. Constraining the stochastic fracture network realizations, also referred as Discrete Fracture Networks (DFN), is expected to improve our predictions of seismo-hydromechanical response of a reservoir during hydraulic stimulation.

The primary motivation of this research is to constrain three dimensional (*3-D)* spatial distribution of fractures in a reservoir using borehole observations. First of all, we start with scaling of fracture patterns in a deep borehole such as Basel-1. We base our analysis on the fractures inferred from acoustic televiewer logs in Basel-1 by Ziegler *et al.* (2015). Then, we use synthetic fracture networks to explore the possible extraction of scaling relationships of *2-D* and *3-D* spatial organizations from *1-D* data.

Methodology

1. Characterization of borehole data: The scaling exponent of fracture patterns (in any dimension) can be computed by fitting a power-law to the corresponding correlation function such as equation 1 where,

$$C(r) = \frac{1}{N^2} N_p(r) \sim r^D \qquad (1)$$

N_p is the number of pairs less than *r* apart,
N the total number of fractures and
r is the distance between two fractures.

2. Generate synthetic networks: According to the literature, the only DFN model with established stereological relationships (i.e. relations among the spatial distributions in one, two and three dimensions) is a dual-power law (Davy *et al.*, 1990, Darcel *et al.*, 2003). This research is focused on performing a critical analysis of such stereological relationships in one and two dimensions, and its possible extension to three dimensions. Equation 2 represents DFN model we apply where,

$$n(l, L).dl = c.L^D l^{-a}.dl \qquad (2)$$

$n(l,,L).dl$ is the number of fractures in the length range of $[l, l + dl]$,
L is the domain length,
D is the correlation dimension,
a is the length exponent with c as a constant.

3. Analyze the possible application of stereological relationships to Constrain DFNs: The process of such an analysis is given in the following flowchart.

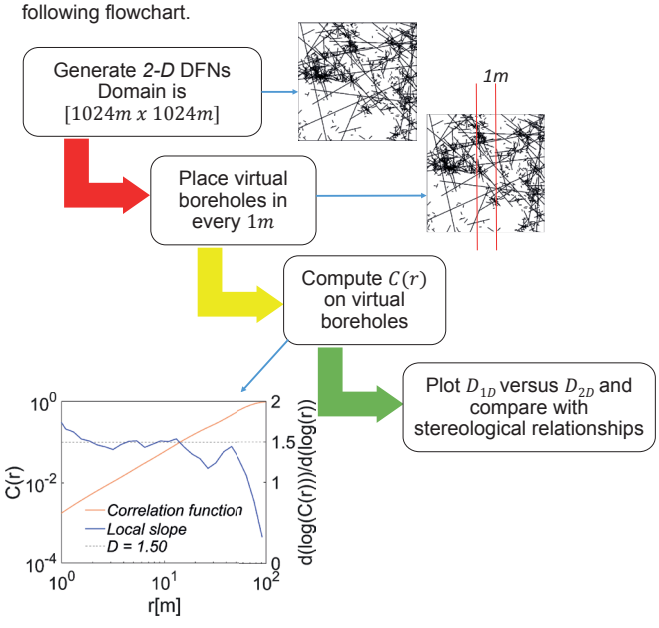

Figure 1. The flowchart of analyzing the application of stereological relationships to Constrain DFNs.

Results

First of all, we present the correlation function of fracture patterns in a deep borehole drilled into crystalline basement (Basel-1). Figure 2 proves the fractal patterns of complete fracture dataset and the dominant fracture set.

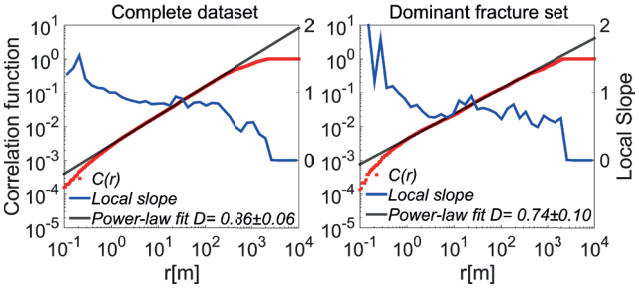

Figure 2. Fractal analysis of the complete fracturing dataset and the dominant fracture set in Basel-1 borehole.

The scale invariance of fracture patterns in Basel-1 might help us to constrain DFNs using available stereological relationships in literature. Figure 3 represents the results of a stereological analysis for two typical length exponents. It is important to note that there is a transition in behaviour of synthetic networks in $a = 2$. Exponents higher than *2,* have a higher frequency of smaller fractures and vice versa.

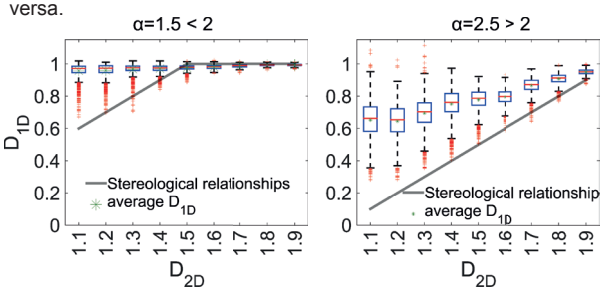

Figure 2. Detailed stereological analysis of synthetic networks in comparison to stereological relationships.

Discussion

- We observed fractal fracture patterns in Basel-1 borehole.
- There is a large discrepancy between the analytical predictions and stereological analysis in synthetic networks.
- The stereological analysis the we performed shows that D_{2D} cannot be reliably estimated from *1-D* data. .
- Estimating *3-D* spatial distribution form one boreholes involves a huge uncertainty associated with estimating D_{2D}. In addition, there is no information about the length distributions of *3-D* fracture planes in the reservoir.

Acknowledgements

The research leading to these results has received funding from the European Community's Seventh Framework Program under grant agreement No. 608553 (Project IMAGE).

References

Ziegler, M., Valley, B., Evans, K. F. (2015). Characterisation of natural fractures and fracture zones of the Basel EGS reservoir inferred from geophysical logging of the Basel-1 well. *World Geothermal Congress Melbourne, Australia*, 19-25.
Davy, P., Sornette, A., Sornette, D. (1990). Some consequences of a proposed fractal nature of continental faulting. *Nature* **348**, 56-58.
Darcel, C., Bour, O., Davy, P. (2003). Stereological analysis of fractal fracture networks. *Journal of Geophysical Research: Solid Earth* **108**.

SCCER SoE
SWISS COMPETENCE CENTER for ENERGY RESEARCH
SUPPLY of ELECTRICITY

SCCER-SoE Annual Conference 2017

In cooperation with the CTI
Energy
Swiss Competence Centers for Energy Research
Schweizerische Eidgenossenschaft
Confédération suisse
Confederazione Svizzera
Confederaziun svizra
Swiss Confederation
Commission for Technology and Innovation CTI

Simultaneous Visualization of Fluid Flow and Mineral Precipitation in Fractured Porous Media

Mehrdad Ahkami, Xiang-Zhao Kong, Martin O. Saar*

Geothermal Energy and Geofluids, Institute of Geophysics, ETH Zurich, Switzerland
** Email: mahkami@ethz.ch*

Background - Motivation

Mineral precipitation during Enhanced Geothermal Systems (EGS) can reduce the efficiency and life time.

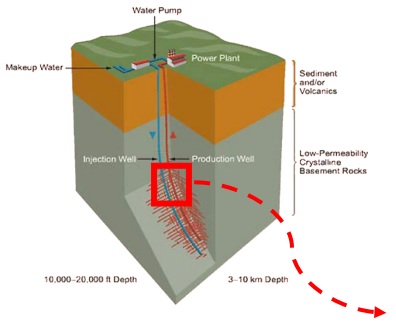

Pore Clogging

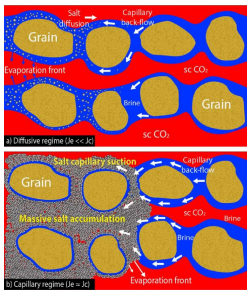

Major causes of mineral precipitation:

- Perturbation of temperature and pressure
- Mixing of two different fluids
- Introducing of a fluid that is out of equilibrium with mineral phase

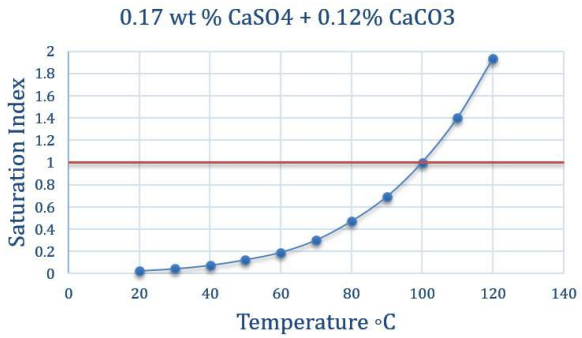

Visualization of Flow by Particle Shadow Velocimetry (PSV)

Fluid is seeded with tracer particles, which are assumed to follow flow dynamics. The motion of seeding particles is illuminated and recorded to determine flow velocity.

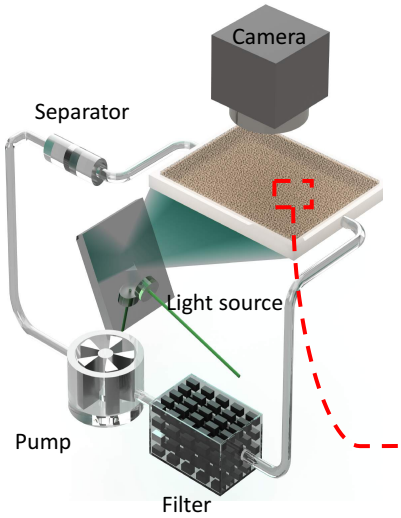

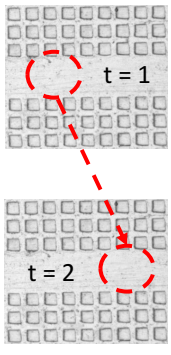

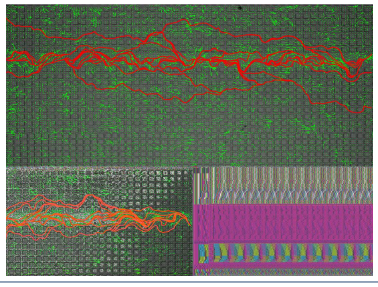

Particle shadow(s) recorded by camera

Lattice Boltzmann simulations, using lbHydra

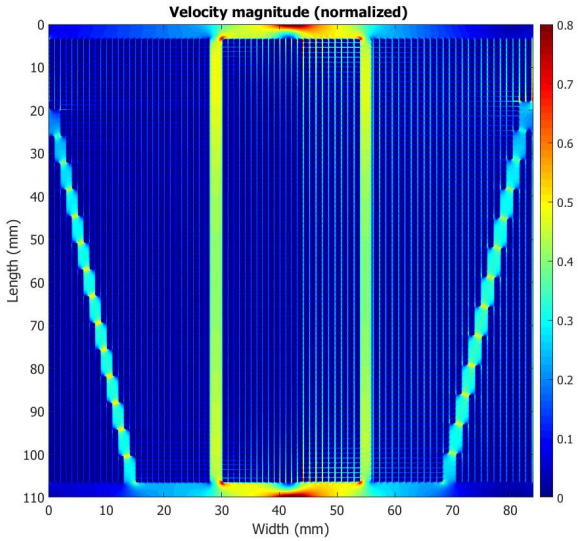

- Lattice Boltzmann method (LBM) was used to calculate the permeability and pressure drop in media to be used in experimental design.
- LBM method was used to design the cell for PSV experiment, to ensure one order of magnitude difference in velocity between fracture and matrix.

Acknowledgement

The project is funded by ETH Research Grant under grant No. ETH-12 15-2.

GEL Geothermal Energy & Geofluids
WSS WERNER SIEMENS-STIFTUNG
ETH Eidgenössische Technische Hochschule Zürich Swiss Federal Institute of Technology Zurich

References:

- Miri, Rohaldin, and Helge Hellevang. "Salt precipitation during CO 2 storage—A review." *International Journal of Greenhouse Gas Control* 51 (2016): 136-147.
- "3 Renewable Electricity Generation Technologies." National Research Council. *Electricity from renewable resources: Status, prospects, and impediments*. National Academies Press, 2010. Page 93

Acoustic monitoring of laboratory hydraulic fracture growth under stress and pore pressure

Thomas E. Blum[1], and Brice Lecampion[1]

[1]Geo-Energy Laboratory — Gaznat chair on Geo-Energy, EPFL, Lausanne, Switzerland

I - Introduction

- Fluid-driven fracturing present in a wide range of applications
  - oil and gas extraction
  - geothermal energy recovery
  - CO2 sequestration
- Need for models to
  - efficiently fracture the targeted rock formation and quantify fracturing
  - better understand the physics of fluid-driven fracturing
  - get an estimate of fracture size and shape during growth
- Theoretical models
  - analytical or numerical solution
  - based on assumptions on fluid and rock properties, geometry...
- Scaled laboratory experiments
  - allow to validate theoretical predictions
  - provide complete datasets of individual experiments performed under controlled conditions
  - include physical limitations
  - history of lab-scale geophysics for geomechanical problems (Hall, 2009)

II - Existing work

- The DelFrac Consortium at TU Delft pioneered this field by building an acoustic monitoring setup inside a triaxial press applying three independent stresses on a cubic specimen (Groenenboom, 1998).
- The CSIRO group in Melbourne also has a triaxial press used for hydraulic fracturing experiments, but mostly uses photometric monitoring methods (Kovalyshen et al., 2014).
- Comparison of existing setups and planned GEL setup

	TU Delft	CSIRO	GEL
Specimen size	300 mm cube	350 mm cube	250 mm cube
Max. stress	30 MPa	25 MPa	20 MPa
Max. injection pressure	50 MPa	75 MPa	50 MPa
Transducers	48	6	64
Frequency	0.5 MHz	1 MHz	1 MHz

- Limitations
  - maximum applicable stress
  - injection rate: controls experiment duration
  - pore pressure? not possible in most setups

III - Laboratory setup

- Planned experimental setup
  - triaxial frame with cubic-shaped specimens of up to 250 mm in length
  - independent stresses on each axis up to 20 MPa
  - pore pressure inside the frame up to 5 MPa
  - high-pressure injection pump with a maximum pressure of 50 MPa
  - flow rate ranging from 1 μL/min to 90 mL/min
  - glued wellbore and notching at the bottom for fracture initiation
- Triaxial cell in testing phase, loaded horizontally

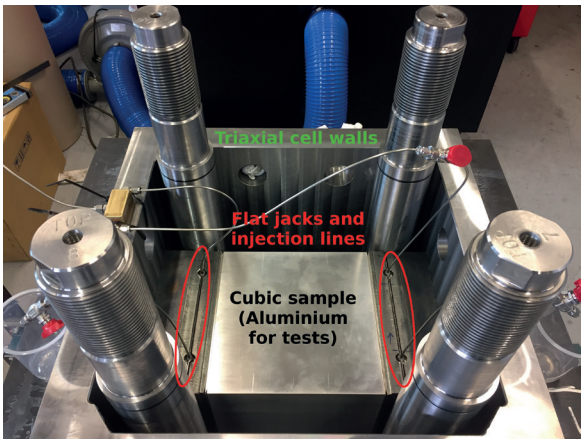

IV - Acoustic monitoring

- Acoustic monitoring setup
  - 54 longitudinal and 10 shear piezoelectric transducers
  - 32 sources swept through a multiplexer
  - function generator and high-power amplifier to create 300 V_{pp} excitation signal
  - 32 receivers connected to high-speed board for simultaneous acquisition at 50 MHz
  - transducers on all sides, most transducers on the sides parallel to the fracture plane
  - full acquisition duration on the order of a few seconds
- Schematic of the triaxial cell with confining stresses, injection line and piezoelectric transducers, simplified propagation modes at bottom right

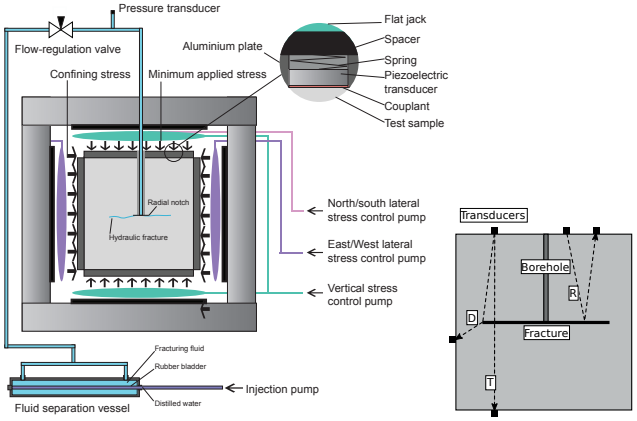

- Wave modes propagating through the sample
  - T: transmitted waves go through the fluid-filled fracture and carry information on the fracture thickness
  - R: waves that are reflected at the fracture interface carry information about the position of the fracture, and also about the occurrence of fluid lag
  - D: waves diffracted from the tip of the fracture carry information about the position of the fracture tip (Groenenboom et al., 2001)
- Thickness estimation (Groenenboom and Fokkema, 1998; Kovalyshen et al., 2014)
  Transmission coefficient for P-waves:

$$T(\omega, h) = \frac{(1 - r_{ff}^2)\exp(i\alpha)}{1 - r_{ff}^2\exp(2i\alpha)} \quad (1)$$

  - h fluid thickness
  - ω wave frequency
  - $r_{ff} = \frac{z_r+1}{z_r-1}$
  - impedance ratio $z_r = \frac{\rho_f c_f}{\rho_s c_s}$
  - ρ_s, ρ_f densities of solid and fracturing fluid
  - c_s, c_f P-wave velocities of solid and fracturing fluid
  - $\alpha = \frac{\omega h}{c_f}$

V - Preliminary results

- Thickness detection test:
  - two PMMA slabs, 125 mm thick, on top of each other
  - water layer in between
  - thickness varies through tightening of a clamp
  - simple transmission measurement with two opposing transducers

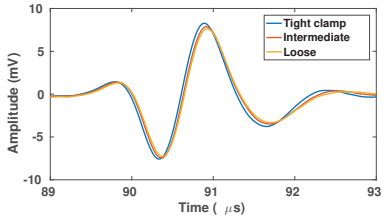

- Thickness changes
  - delayed arrival when fluid thickness increases due to travel through fluid layer
  - but also decreased amplitude: change in transmission coefficient

VI - Future applications

- Investigation of the process zone in quasi-brittle materials
- Fracture propagation in anisotropic or inhomogeneous materials
- Effects of mixed-mode fracturing with fracture reorientation
- Fracture profile for different fluid types: Newtonian, "power-law" ...

VII - Conclusion

- Unique experimental capabilities with triaxial stresses and pore pressure
- Dense ultrasonic monitoring for improved fracture geometry estimation
- Growing list of applications
- Full operation expected end of 2017!

References

J. Groenenboom. *Acoustic monitoring of hydraulic fracture growth*. PhD thesis, TU Delft, 1998.

J. Groenenboom and J. T. Fokkema. Monitoring the width of hydraulic fractures with acoustic waves. *Geophysics*, 63:139–148, 1998.

J. Groenenboom, D. B. van Dam, and C. J. de Pater. Time-Lapse Ultrasonic Measurements of Laboratory Hydraulic-Fracture Growth: Tip Behavior and Width Profile. *SPE Journal*, 6(01):14–24, Mar. 2001.

S. A. Hall. When geophysics met geomechanics: Imaging of geomechanical properties and processes using elastic waves. In D. Kolymbas and G. Viggiani, editors, *Mechanics of Natural Solids*, pages 147–175. Springer Berlin Heidelberg, 2009.

Y. Kovalyshen, A. P. Bunger, J. Kear, and D. Kasperczyk. Comparison between ultrasonic and photometric methods for hydraulic fracture laboratory monitoring. *International Journal of Rock Mechanics and Mining Sciences*, 70:368–374, Sept. 2014.

http://gel.epfl.ch thomas.blum@epfl.ch

SCCER SoE
SWISS COMPETENCE CENTER for ENERGY RESEARCH
SUPPLY of ELECTRICITY

SCCER-SoE Annual Conference 2017

In cooperation with the CTI
Energy
Swiss Competence Centers for Energy Research
Schweizerische Eidgenossenschaft
Confédération suisse
Confederazione Svizzera
Confederaziun svizra

Cross-borehole characterization of permeability enhancement & heat transport in stimulated fractured media : preliminary results from the ISC experiment at the Grimsel Test Site

Bernard Brixel*, Maria Klepikova*, Mohammadreza Jalali*, Florian Amann*, Simon Loew*
*Institute of Geology, Group of Engineering Geology, NO Building, Sonneggstrasse 5, ETHZ, 8092 Zurich

Motivation

1. Detect and characterize permeability enhancement in response to hydro-shearing
2. Understand the effects of stimulation on fluid flow and heat transport
3. Identify the permeable fractures that contribute to heat transport

Approach & Concepts

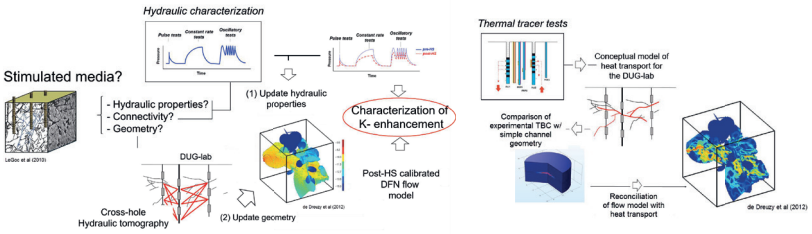

Fig. 1 Proposed in-situ methods and numerical approach

Methods

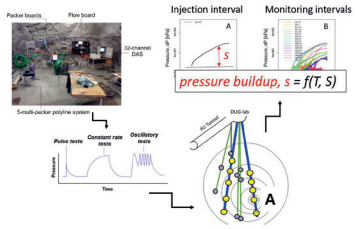

Fig. 3. Injection test procedure & monitoring

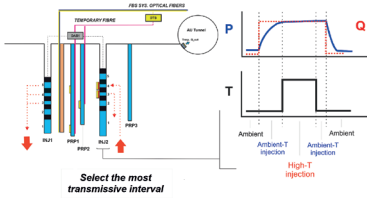

Fig. 4. Heat tracer test procedure & monitoring

Geology & Site layout

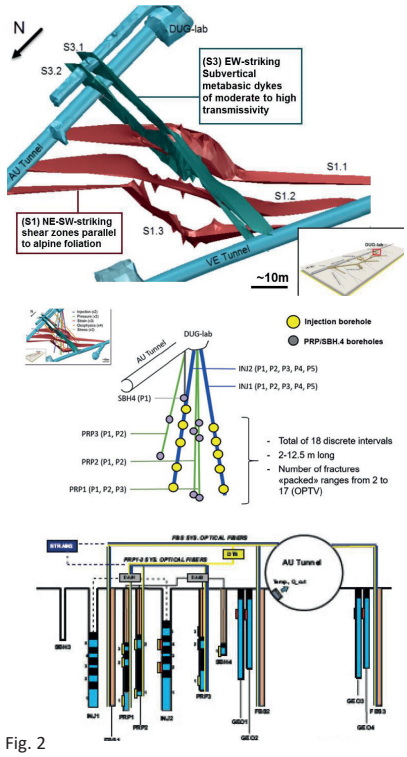

Fig. 2

Preliminary field results

Permeability enhancement

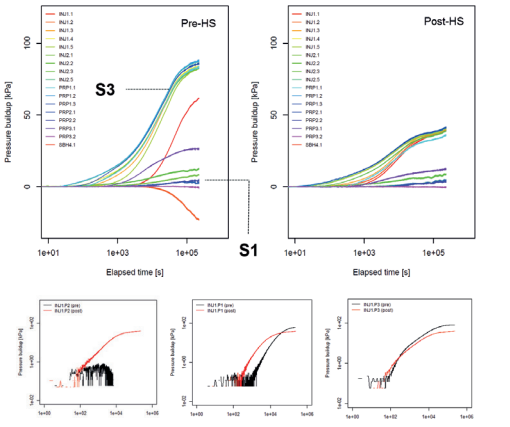

Fig. 5. Pressure transients in response to a constant rate injection test, pre vs. post- hydraulic stimulation

Heat transport

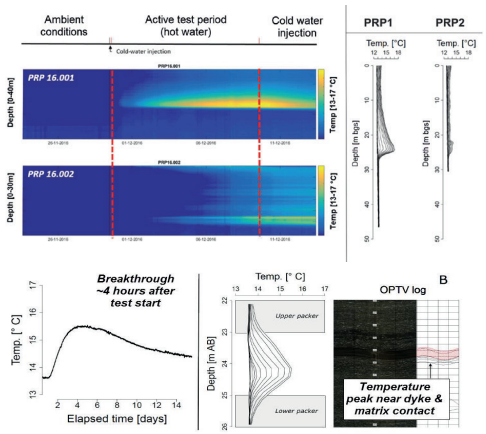

Fig. 6. Thermal breakthroughs and temperature profiles in open boreholes (top) vs packed-off interval (bottom)

Conclusions

1. Pressure transients from hydraulic tests completed following the same procedure, both before and after hydraulic shearing, show that the connectivity of the fracture network increased, at least over a scale of 10 m.
2. Both NEW and ENHANCED connections have been detected through hydraulic testing (see Fig. 5).
3. The propagation of heat during thermal tracer tests is constrained to discrete flow pathways (see Fig. 6), which helps us identifying the permeable fractures that contributing to heat transport.

Effect of fluid viscosity on fault frictional behavior

Chiara Cornelio[1], Elena Spagnuolo[2], Giulio Di Toro[3] and Marie Violay[1]

[1] Laboratory of Experimental Rock Mechanics, EPFL, Lausanne, Switzerland
[2] Istituto Nazionale di Geofisica e Vulcanologia, Rome, Italy
[3] School of Earth, Atmospheric and Environmental Science, University of Manchester

Introduction

Tectonic fault are often lubricated by viscous fluid which can have different nature e.g. gas, water, brine, melt and viscosities varying over 7 order of magnitude (from 10^{-4} for water to 10^{3} $Pa \cdot s^{-1}$ for melt at high temperature). Moreover, understanding fluids viscosity effects on fault dynamics can shed light on the induced seismicity in engineering reservoirs where fluids with viscosity ranking from $1 mPa \cdot s^{-1}$ to $1000 mPa \cdot s^{-1}$ are also injected during hydraulic fracturing process in order to increase the permeability. Here, we examine the mechanisms coming into play in presence of viscous lubricant film between the rock slip surfaces during both earthquake nucleation (slip rate from $\mu m \cdot s^{-1}$ to $mm \cdot s^{-1}$) and propagation ($mm \cdot s^{-1}$ to $m \cdot s^{-1}$) where mixed lubrication and fully lubricated regime might be activated, using rotary shear tests on precut samples of Westerly granite.

SHIVA Set-Up

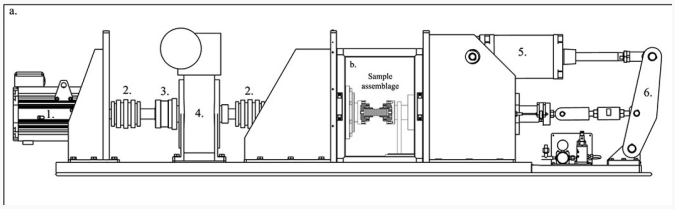

Figure 1: Slow to HIgh Velocity Apparatus. (a) 1. Large electric motor. 2. Bellow couplings. 3. Sprag clutch. 4. Gear box. 5. Air actuator. 6. Steel arm to amplify the axial load. The axial load is imposed by the air actuator and monitored by a computer. The torque is measured using a torque bar.

Table of Experiments

V[mm/s]	H_2O	60%glyc	85%glyc	99%glyc
10^{-2}	s1318	s1312	s1306	\
10^{-1}	s1319	s1313	s1309	\
10^{0}	s1302	\	s1304	\
10^{1}	s1320	s1315	s1308	s1387
10^{2}	s1386	s1317	s1311	s1388
10^{3}	s1303	s1316	s1305	s1389

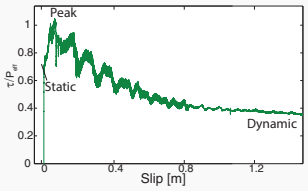

Results

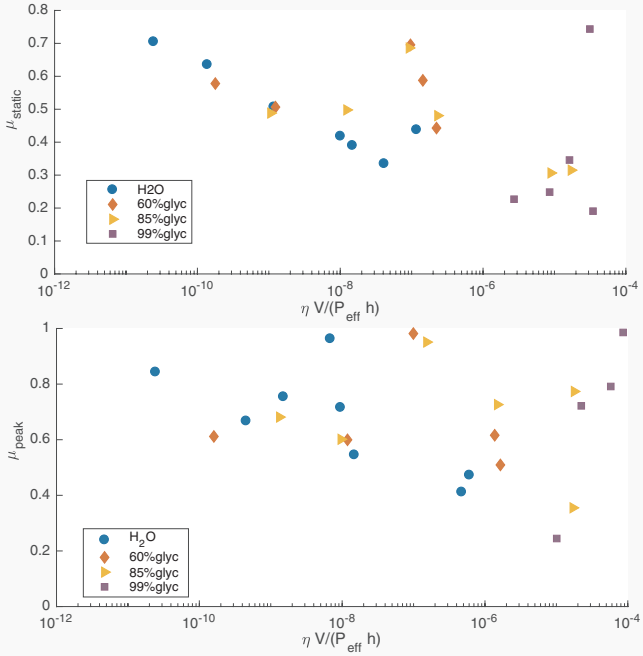

Figure 2: Static and Peak friction coefficient vs Sommerfield number

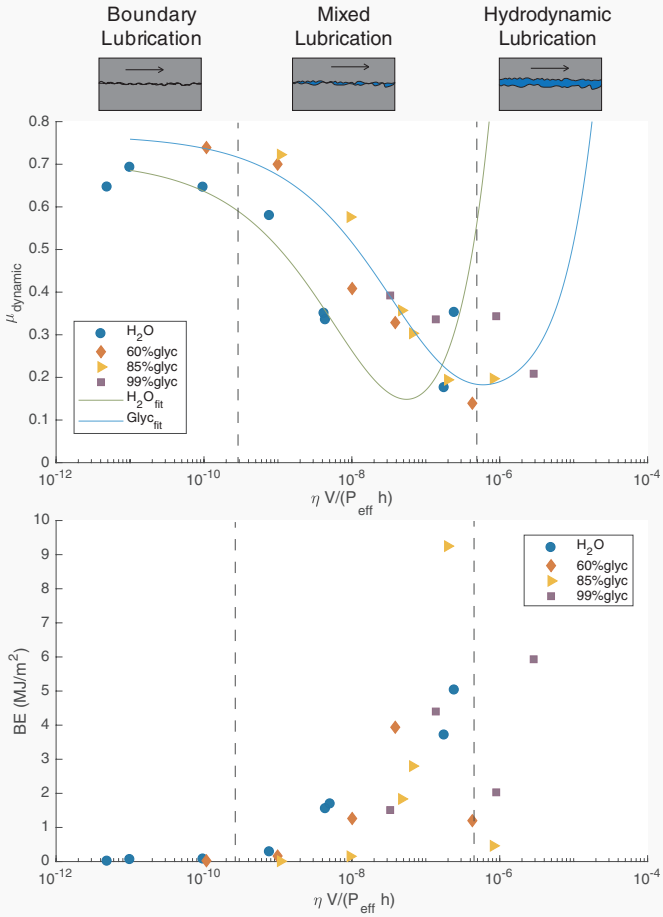

Figure 3: Dynamic friction coefficient and Frictional energy vs Sommerfield number

Conclusion

	μ_{static}	μ_{peak}	$\mu_{dynamic}$	B_E
Presence of fluid	Yes	No	Yes	Yes
Type of fluid	No	No	Yes	No
$\nearrow \eta$	$\searrow$	No	$\searrow$	$\nearrow$
$\nearrow V$	$\searrow$	Slightly	$\searrow$	$\nearrow$

- 30 tests in rotary shear apparatus have been performed, using different viscous fluid and imposing different target slip rate
- Three different lubricated regime have been detected
- Static friction coefficient is strongly dependent on fluid viscosity
- Dynamic friction coefficient is strongly dependent on fluid rheology and viscosity
- Frictional energy does not depend on the nature of the fluid, but it depends on fluid viscosity and velocity
- It increases in boundary and mixed regimes
- It abruptly decreases in fully lubricated regime
- Lubrication $\neq$ Easy EQ Propagation

References

Brodsky, E. E. Kanamori, H. *Elastohydrodynamic lubrication of faults.* J. Geophys. Res. 106, 16,357-16,374 (2001).
Di Toro, G. et al. *Fault lubrication during earthquakes.* Nature 471, 494â498 (2011).
Persson, B. *Sliding Friction. Physical Principles and Applications.* Springer-Verlag Berlin Heidelberg, 2000. doi:10.1007/978-3-662-04283-0

SCCER SoE
SWISS COMPETENCE CENTER for ENERGY RESEARCH SUPPLY of ELECTRICITY
unine UNIVERSITÉ DE NEUCHÂTEL
ETH zürich

SCCER-SoE Annual Conference 2017

In cooperation with the CTI
Energy Swiss Competence Centers for Energy Research
Schweizerische Eidgenossenschaft Confédération suisse Confederazione Svizzera Confederaziun svizra
Swiss Confederation
Commission for Technology and Innovation CTI

Injection Protocol and First Results of Hydraulic Fracturing Experiments at the Grimsel Test Site

Nathan Dutler*, Benoît Valley*, Linus Villiger**, Hannes Krietsch***, Mohammedreza Jalali***, Valentin Gischig***, Joseph Doetsch*** & Florian Amann***
*Centre for Hydrogeology and Geothermics, University of Neuchâtel, Rue Emile-Argand 11, CH-2000 Neuchâtel
** Swiss Seismological Service, ETH Zurich, Sonneggstrasse 5, CH-8092 Zurich
*** Department of Earth Sciences, ETH Zurich, Sonneggstrasse 5, CH-8092 Zurich

Motivation

Hydraulic fracturing (HF) is a common method to create artificial fractures to create new flow paths and to connect to pre-existing fractures. We aim to study injection parameters, such as injection flow rate and fluid viscosity, and their influence on fracture propagation, fracture geometry and micro-seismicity in crystalline rock.
The HF experiments are part of the in-situ stimulation and circulation project (Amann et al., 2017), which was recently carried out at the Grimsel Test Site.

Propagation mode of hydraulic fractures

- Numerical modelling has been used to study the size and mode (toughness or viscosity dominated) of the growing fractures
- A penny-shaped fracture geometry is assumed due to model calibration with hydraulic fractures during stress characterization phase.
- Definition of fracture toughness value for determining the asymptotes:

$$K = K' \times \left(\frac{t^2}{E'^3 \mu'^5 Q^3}\right)^{\frac{1}{18}}$$

K' fracture toughness value
t time
E' plane-strain modulus
μ' fluid viscosity
Q flow rate

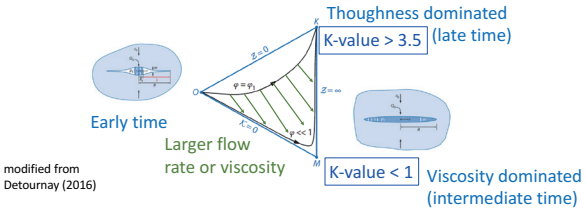

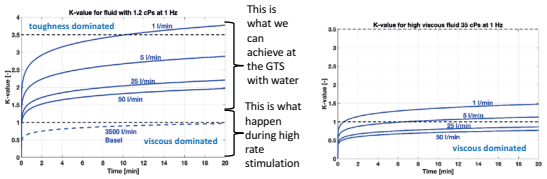

Figure 1: Propagation mode of penny-shaped hydraulic fractures

- To achieve similar behavior than for high rate stimulation, the fluid viscosity was increased using a rheology modifier (i.e. Xanthan Gum Keltro T622 at a 0.025%wt resulting in an expected viscosity of 35-40 cPs at a shear rate of 1 Hz).
- Expected fracture length in ideal isotropic rock is between 25 and 30 m depending on the injection fluid viscosity.

Hydraulic fracture growth in previous experiments (Gischig et al., 2017)

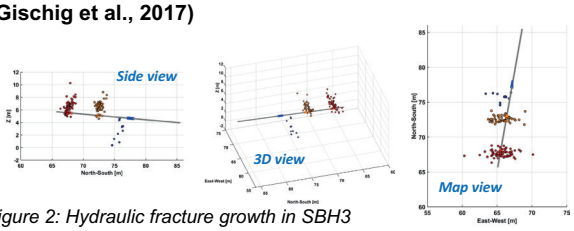

Figure 2: Hydraulic fracture growth in SBH3 borehole observed by micro-seismic monitoring

- Small injection flow rates were used (1-5 lpm)
- Impression packer show an opening along the foliation plane (157/75°)
- Micro-seisimic monitoring show fracture propagation in E-W direction

Injection protocol

- Injection of ~1 m³ fluid for each injection phase
- The injection protocol includes the following elements:
  1. Initial pulse tested to verify packed interval integrity
  2. A formation breakdown test at relatively low flow rate (i.e. 5 lpm)
  3. A main fracture propagation phase with flow rates up to 100 lpm. Two cycles are used to reach high flow rates due to pump change at 35 lpm. Flushing is added to the high viscous gel injection protocol (Figure 3B).
  4. A pressure rate test to measure the stress normal to the created fracture

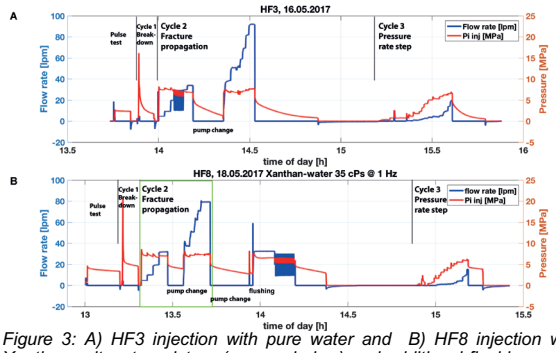

Figure 3: A) HF3 injection with pure water and B) HF8 injection with Xanthan-salt-water-mixture (green window) and additional flushing cycle. The flow rate is indicated by the blue solid line and the corresponding interval pressure is red.

The breakdown pressure for HF3 was at 16.2 MPa. The jacking pressure measured 5.8 MPa and the final injectivity measured 0.88 l/min/MPa. The break down pressure for HF8 was at 21.1 MPa and the jacking pressure measured 5.0 MPa. The final injectivity measures 0.20 l/min/MPa. For all HF-experiments the injectivity increased 100 to 1000 times.

Preliminary Insights

1. HF connects to pre-existing fractures such that the fracture fluid leak-off. Further fracture propagation is leaded by hydraulic shearing due to hitting a pre-existing system. The effect of shearing is depended on the fluid (flow rate and viscosity) and the early stage fracture orientation/geometry.
2. Likelihood to create single flow path rather than flow volume.
3. Evidence for creating a temporary hydraulic connection to the fracture system that closes after stimulation.
4. The injectivities after HF are around 0.1 to 1 l/min/MPa. These are similar to the HS-experiments.
5. The prediction of E-W fracture propagation needs to be validated by the microseismic cloud and the opening along the foliation plane is yet not be validated by acoustic televiewer log.

References

- Amann, F., et al. (2017), The seismo-hydro-mechanical behaviour during deep geothermal reservoir stimulation: open questions tackled in a decameter-scale in-situ stimulation experiment. Solid Earth Discuss., https://doi.org/10.5194/se-2017-79
- Detournay, E. (2016). Mechanics of Hydraulic Fractures. In Davis, SH and Moin, P, (eds), Annual Review of Fluid Mechanics, vol 48, p. 311-339.
- Gischig, V.S., Doetsch, J., Maurer, H., Krietsch H., Amann F., Evans, K.F., Nejati, M., Jalali, M., Valley, B., Obermann, A., Wiemer, S. and Giardini, D. (2017), On the link between stress field and small-scale hydraulic fracture growth in anisotropic rock derived from microseismicity. Solid Earth Discuss., https://doi.org/10.5194/se-2017-78

Email: nathan.dutler@unine.ch

SCCER SoE
SWISS COMPETENCE CENTER for ENERGY RESEARCH
SUPPLY of ELECTRICITY

SCCER-SoE Annual Conference 2017

In cooperation with the CTI
Energy
Swiss Competence Centers for Energy Research
Schweizerische Eidgenossenschaft
Confédération suisse
Confederazione Svizzera
Confederaziun svizra
Swiss Confederation
Commission for Technology and Innovation CTI

Impact of CO_2 injection on the hydro-mechanical behaviour of a clay-rich caprock

Valentina Favero and Lyesse Laloui

Introduction

Research of the chair "Gaz Naturel" – Petrosvibri at the EPFL contributes to SCCER-SoE WP1: "DGE and CO_2 sequestration". WP1 research focuses on problems for future realization of CO_2 storage in Switzerland. Proper assessment of carbon dioxide storage procedures allows to significantly reduce its concentration in the atmosphere and thus directly contributes to Swiss energy strategy 2050. The sound characterization of reservoirs and caprocks in Switzerland and the assessment of their potential for CO_2 storage is therefore fundamental.

In order to grant a safe injection of CO_2 into reservoir formations, the overlaying shaly caprock must perform efficiently. This work aims at identifying the relevant processes related to shale-CO_2 interactions and the impact of CO_2 injection on the mechanical properties of the material.

Experimental methodology

Cylindrical specimens of intact Opalinus Clay shale :
- height ≈ 12.5 mm
- diameter = 35 mm

An advanced oedometric system (imposing zero lateral strain) is used (Figure 1).

Procedure for Test 1 and Test 2:
- Saturation in constant volume conditions;
- Pore water pressure increase to 7.3 MPa while maintaining constant vertical effective stress;
- Consolidation in steps to the desired stress state;
- CO_2 injection at liquid state (23°C, pressure up to 12 MPa)
- Mechanical compression up to 90 MPa of vertical total stress.

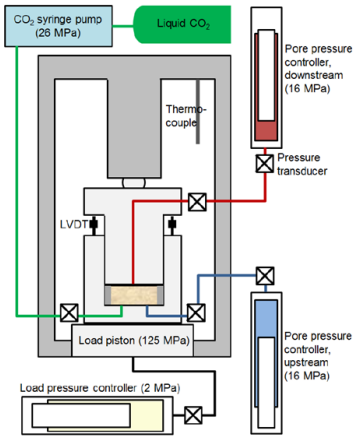

Figure 1: Advanced oedometric system.

The stress paths of the tests are depicted below:

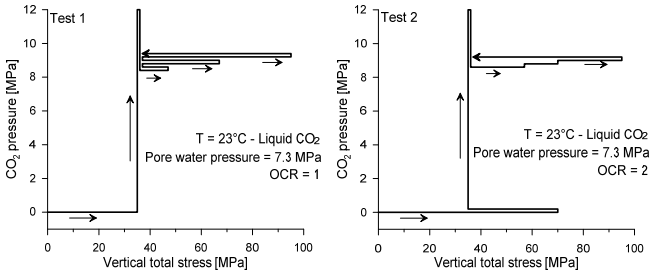

Results

Vertical strain versus vertical effective stress during oedometric loading and during CO_2 injection at constant vertical effective stress.

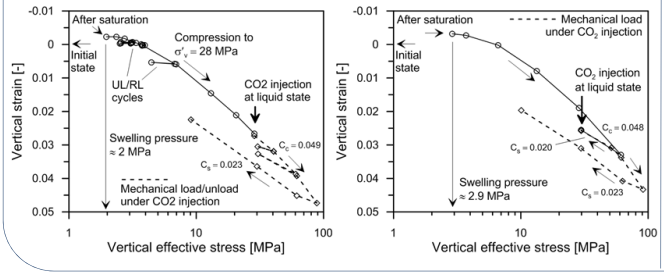

Results and Discussion

Loading (test 1) and unloading (test 2) steps prior to CO_2 injection (black solid line), followed by the CO_2 injection phase (red line)

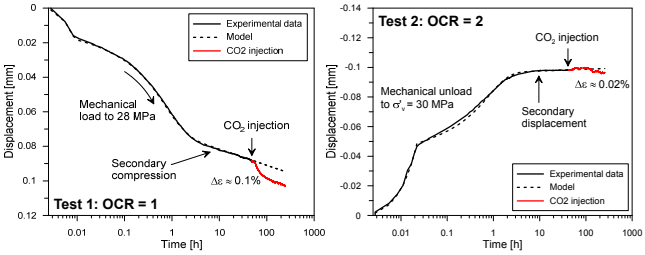

Strain induced by CO_2 injection is relevant at OCR = 1
→ material structure is more prone to collapse when it is found in normally consolidated conditions.

Details of the CO_2 injection phase:

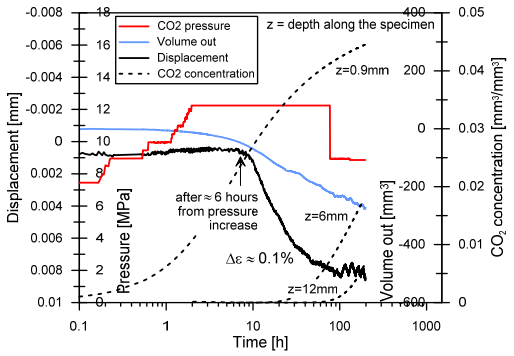

Possible causes of strains induced by CO_2 injection:
→ Desaturation effects (CO_2 / pore water differential pressure)
→ Double layer effects induced by the diffusion of CO_2

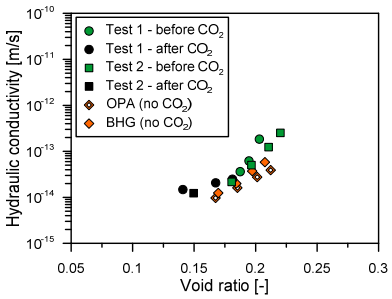

The impact of CO_2 injection on the deformation behaviour of the material appears to be limited compared to the deformation behaviour induced by a mechanical loading.

Diffusion of CO_2 into the shale does not impact significantly the hydro-mechanical properties of the material, since no significant change in oedometric modulus and hydraulic conductivity are highlighted after the injection of CO_2.

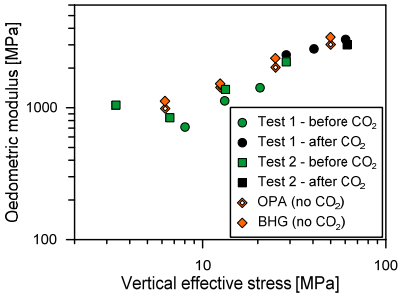

Acknowledgement

V. Favero is an SCCER-SoE postdoctoral researcher. The tested shale is provided by Swisstopo.

SCCER SoE
SWISS COMPETENCE CENTER for ENERGY RESEARCH
SUPPLY of ELECTRICITY

SCCER-SoE Annual Conference 2017

In cooperation with the CTI
Energy
Swiss Competence Centers for Energy Research
Schweizerische Eidgenossenschaft
Confédération suisse
Confederazione Svizzera
Confederaziun svizra
Swiss Confederation
Commission for Technology and Innovation CTI

Visualizing salt tracers using GPR

Peter-Lasse Giertzuch, Joseph Doetsch*, Alexis Shakas**, Mohammadreza Jalali*, Anniina Kittilä*, Hansruedi Maurer**
* Department of Earth Sciences, ETH Zurich, CH-8092 Zurich; ** Institute of Earth Sciences, University of Lausanne, CH-1015 Lausanne

Motivation

Hydraulic tracer tests are a powerful tool to characterize connections between subsurface locations, but the actual flow path remains unresolved. One potential method to investigate this is presented here and relies on Ground Penetrating Radar (GPR) and salt tracers. The experiments described here were conducted within the ISC project at the the Grimsel Test Site (GTS).

Single-Hole Reflection GPR

The GPR reflection response is sensitive to electrical conductivity and permittivity. At interfaces with changing parameters, a signal reflection occurs. This way structural changes, i.e. shear zones, can be imaged.

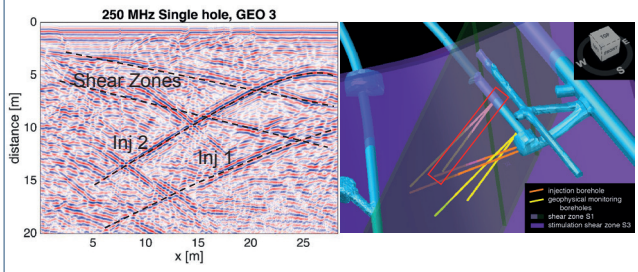

For single-hole reflection GPR the transmitter and the receiver were moved with a fixed distance in the same borehole. Every 5 cm a trace is recorded, which adds up to a reflection image. The acquisition was performed with 250 MHz antennas in borehole GEO 3, indicated in red on the schematics. Amongst other reflections, the structures from the shear zones and the two injection lines are well visible in the data.

Salt Tracer for GPR

Salt water changes the electrical conductivity locally, hence induces a signal change. As salt water has a higher density than tap water, ethanol is added to achieve a neutrally buoyant tracer to achieve comparability with other tracer tests.

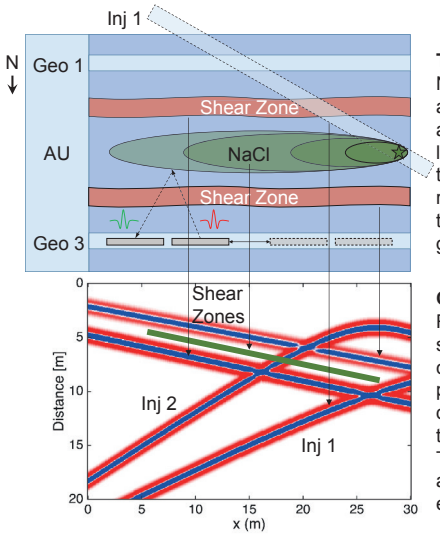

Top view schematics. Note: The shear zones and the boreholes have an inclination and do not lie parallel as drawn in the schematics. The reflection image shows the result from the real geometry.

Calculated model. Reflections from the shear zones occur from changes in the permittivity, due to a different water content than the surroundings. The tracer reflection arises from a change of electrical conductivity.

The tracer used here is composed of: 85 kg water, 21 kg ethanol and 4.5 kg of salt, which leads to a conductivity of 31.8 mS/cm. It was injected in injection line 1 of the GTS over a course of 90 min with tap water and two dye tracers injected before and after for later comparison.

Difference Imaging

The salt tracer only induces small changes in the GPR reflection image. To retrieve the tracer information, a reference image is acquired before tracer injection. The difference between the following measurements and the reference should leave only the tracer visible. Small variations in the data, especially time or phase shifts, have a large impact on the differences. The following processing steps were used to correct for these issues:

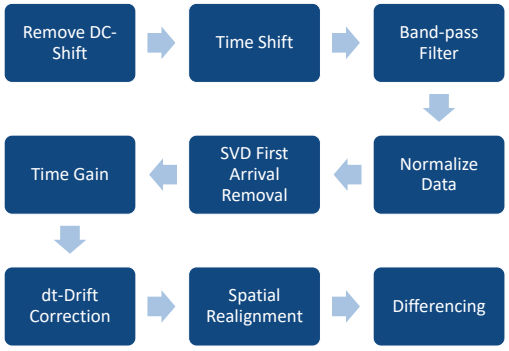

Results

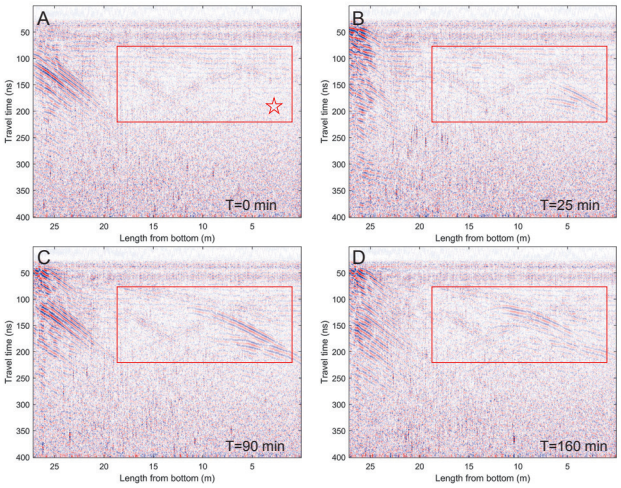

Difference images at increasing time from A to D. The borehole and shear zone reflections are mostly eliminated by the differencing. Artifacts on the top left of the images arise from effects in the tunnel.

A: Tracer not yet visible.
B: Tracer visible at injection point (indicated in A).
C: Tracer propagates.
D: Tracer propagates further and starts to vanish from dilution.

Conclusion & Outlook

The current state of the project proves that salt tracers can be used to monitor tracer movement using GPR. Together with additional information from hydraulic tracer tests, more information on the flow path, the media porosities and tracer velocities can be gained. In the future the GPR data with integration of hydraulic tracer test results will be used to generate a hydraulic model of the ISC project volume.

Email: peter-lasse.giertzuch@erdw.ethz.ch

SCCER SoE
SWISS COMPETENCE CENTER for ENERGY RESEARCH
SUPPLY of ELECTRICITY

ETH zürich

SCCER-SoE Annual Conference 2017

In cooperation with the CTI
Energy
Swiss Competence Centers for Energy Research
Schweizerische Eidgenossenschaft
Confédération suisse
Confederazione Svizzera
Confederaziun svizra
Swiss Confederation
Commission for Technology and Innovation CTI

A comparison of the seismo-hydro-mechanical observations during two hydraulic stimulation at the Grimsel Test Site

Valentin Gischig*, Joseph Doetsch*, Mohammadreza Jalali*, Florian Amann*, Hannes Krietsch*, Linus Villiger**, Nathan Dutler***, Benoît Valley***
* Department of Earth Sciences, ETH Zurich, CH-8092 Zurich; ** Swiss Seismological Service, ETH Zurich, CH-8092 Zurich
***Centre for Hydrogeology and Geothermics, University of Neuchâtel, CH-2000 Neuchâtel

Stimulation interval HS4 at 27.2 - 28.2 m in borehole INJ1, S3 shear zone

Stimulation interval HS1 at 39.75 - 40.75 m in borehole INJ2, S1 shear zone

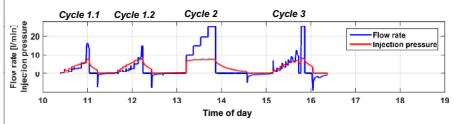

Injection strategy

Cycle 1.1: Pressure –controlled, determination of initial injectivity, breakdown of rock

Cycle 1.2: Pressure –controlled, determination of jacking pressure

Cycle 2: Rate-controlled, actual stimulation

Cycle 3: Pressure –controlled, determination of final injectivity and jacking pressure

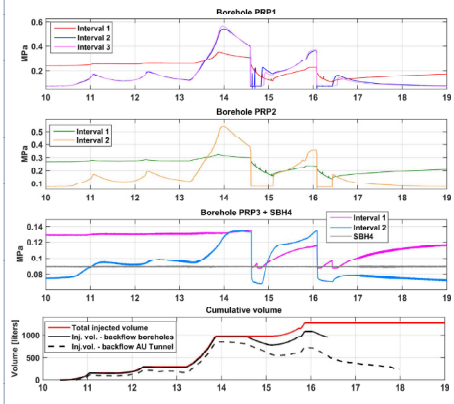

Pressure monitoring

A total of 12 pressure observation intervals to record pressure evolution

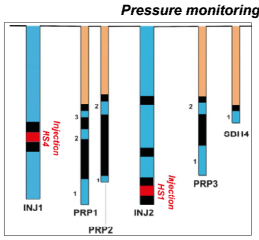

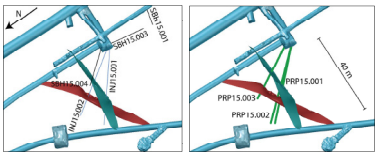

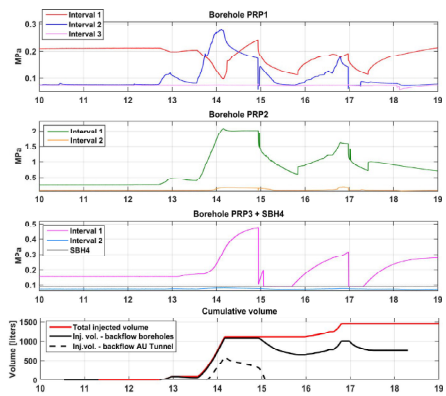

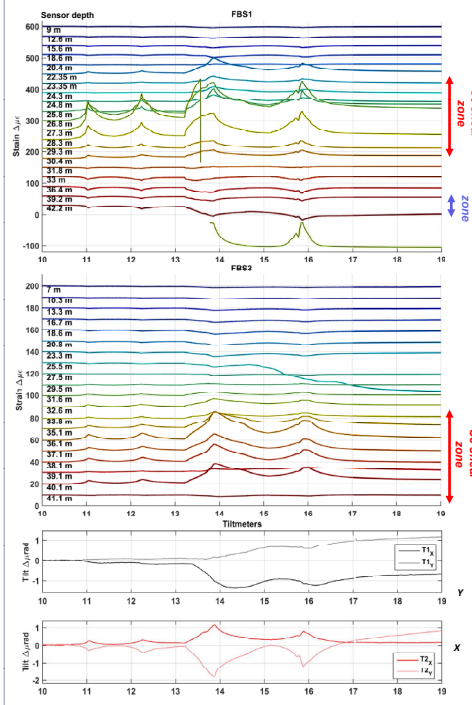

Deformation monitoring

Longitudinal strain with fibre-optics sensors
60 FBG sensors and distributed strain sensing cable in 3 boreholes

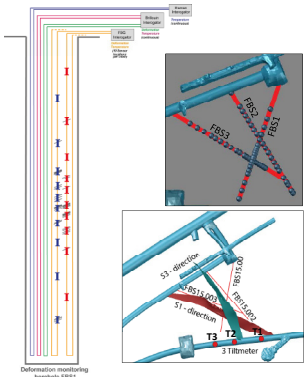

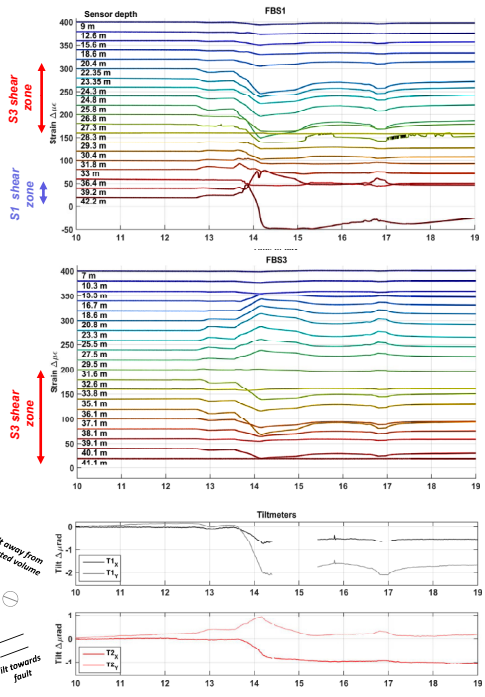

3 horizontal tiltmeters

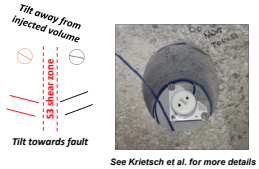

See Krietsch et al. for more details

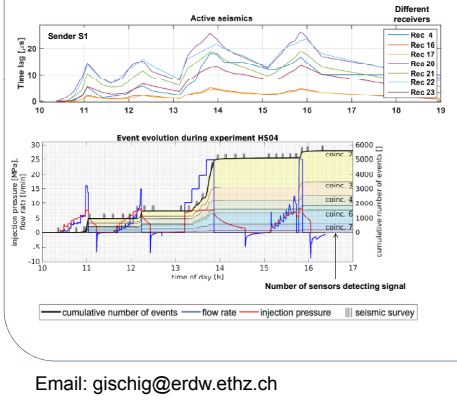

Active + passive seismics

Systematic travel time changes in the stimulated volume
Variable number of seismic events

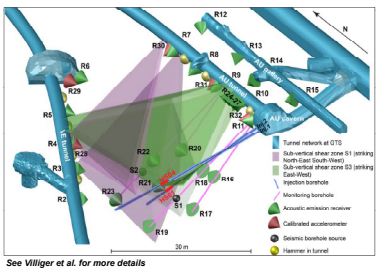

See Villiger et al. for more details

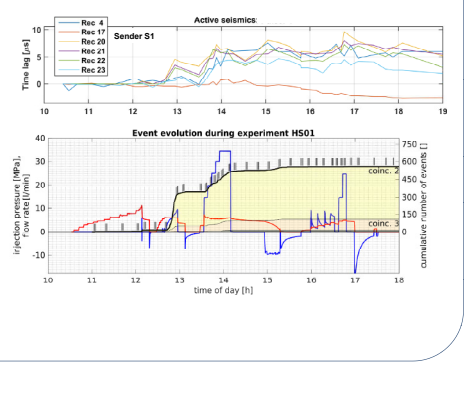

Email: gischig@erdw.ethz.ch

SCCER SoE
SWISS COMPETENCE CENTER for ENERGY RESEARCH
SUPPLY of ELECTRICITY

SCCER-SoE Annual Conference 2017

In cooperation with the CTI
Energy
Swiss Competence Centers for Energy Research
Schweizerische Eidgenossenschaft
Confédération suisse
Confederazione Svizzera
Confederaziun svizra
Swiss Confederation
Commission for Technology and Innovation CTI

Permeability Changes Induced by Hydraulic Stimulation at the Grimsel Test Site

Mohammadreza Jalali, Valentin Gischig*, Joseph Doetsch*, Hannes Krietsch*, Linus Villiger**, Nathan Dutler***, Benoît Valley***, Keith F. Evans**, Florian Amann**

* Department of Earth Sciences, ETH Zurich, Sonneggstrasse 5, CH-8092 Zurich
** Swiss Seismological Service, ETH Zurich, Sonneggstrasse 5, CH-8092 Zurich
*** Centre for Hydrogeology and Geothermics, University of Neuchâtel, Rue Emile-Argand 11, CH-2000 Neuchâtel

Introduction

In-situ stimulation and circulation (ISC) experiment is a unique decameter stimulation experiment which was initiated at the Grimsel Test Site (GTS) in August 2015 [Amann et al., 2017]. The main objective of the ISC experiment is improving our understanding of the thermo-hydro-mechanical and seismic (THMS) processes during hydraulic stimulation of crystalline rocks. In particular, we are interested in

- The creation of sustainable heat exchanger via permanent hydraulic conductivity enhancement during high-pressure fluid injection
- Ways to maximize the ability to assess, model and control induced seismic hazard and risk.

A series of hydraulic stimulation tests had been executed as part of the ISC experiment to fulfill the objectives, which are (Figure 1, Table 1):

- Ten mini hydraulic fracturing (MHF) and one hydraulic testing in pre-existing fractures (HTPF) in SBH boreholes (September 2015)
- Six hydraulic shearing (HS) in INJ boreholes (February 2017)
- Six hydraulic fracturing (HF) in INJ boreholes (May 2017)

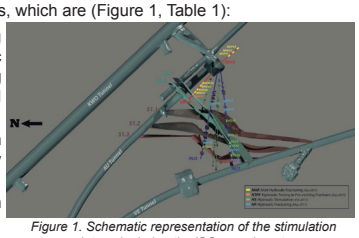

Figure 1. Schematic representation of the stimulation intervals during the ISC experiment.

In this study, the effect of these multi-scale hydraulic stimulation on permeability enhancement and injectivity increment of the rock volume is studied.

Hydraulic Stimulation Mechanisms

Hydraulic stimulation describes two distinct but related mechanisms, which are

(1) initiation and propagation of new fractures (mode I fractures), so-called ***hydraulic fracturing (HF)***, and
(2) shearing of pre-existing fractures (mode II and III), i.e. ***hydraulic shearing (HS)*** (Figure 2).

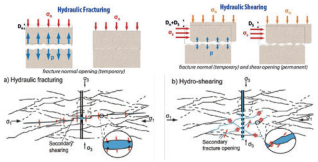

Figure 2. Hydraulic fracturing and hydraulic shearing mechanisms

The occurrence of dominant mechanisms depends on ***rock mass properties*** such as ***rock mass structure***, ***in-situ stress condition***, the ***orientation of existing structures*** such as fractures, faults, and foliation as well as the ***injection properties*** such as ***injection rate*** and ***fluid viscosity***.
In reality, shearing as well as fracture formation and opening may occur concomitantly, and the distinction between them during injection is challenging.
A major difference between HF and HS is the resultant permeability enhancement; it tends to be irreversible for HS but is mostly reversible for HF as the fractures almost fully close after depressurization.

Permeability Changes During Stress Measurement

Ten mini hydraulic fracturing and one HTPF test were performed in three stress measurement boreholes, i.e. SBH1, SBH3, and SBH4 in order to estimate the orientation and magnitude of the principal stresses in the stimulated rock volume [Krietsch et al., 2017]. To determine the impact of these meter-scale hydraulic stimulations in the SBH3 and SBH4 boreholes, permeability, storativity and flow regime of each test were measured before and after the stress measurement using the conventional packer tests [Jalali et al., 2017].

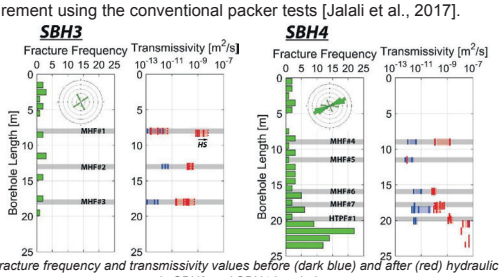

Figure 3. Fracture frequency and transmissivity values before (dark blue) and after (red) hydraulic fracturing in SBH3 and SBH4 boreholes.

Permeability Changes During Hydraulic Shearing and hydraulic Fracturing

Hydraulic stimulation during ISC experiment consists of two parts:

- High-pressure water injection into existing faults and fracture zones within the test volume so that the effective normal stress on the structures is reduced and hydraulic shearing is triggered → Hydraulic Shearing (HS)
- High-pressure water and Xanthan injection into fracture-free borehole intervals so as to initiate and propagate hydraulic fractures → Hydraulic Fracturing (HF)

Permeability and transmissivity changes as a result of hydraulic stimulation were measured using step-pressure tests as well as conventional packer tests (Figure 4 & 5).

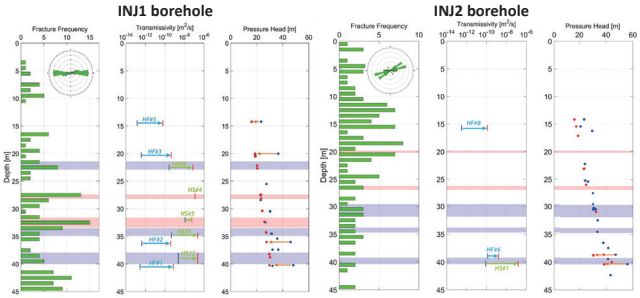

Figure 4. Fracture frequency, transmissivity and pressure head values before (dark blue) and after (red) hydraulic stimulations in two injection boreholes.

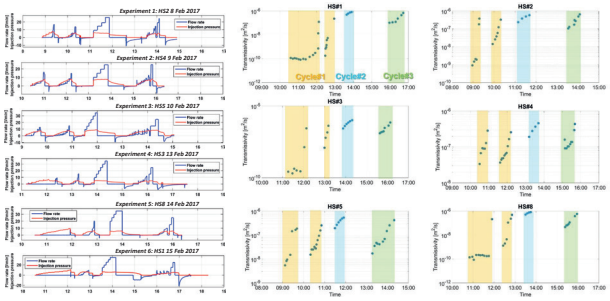

Figure 5. Transient transmissivity changes as a response to injection pressure and flow rate during six hydraulic shearing tests

Table 1. Summary of all the hydraulic stimulation tests conducted during the ISC experiment

Borehole	Test	Structure	Injected Volume [lit]	Initial Trans. [m²/s]	Final Trans. [m²/s]	Change in Trans.	Detected Events
SBH3	MHF#1	---	7.9	3.8E-13	1.5E-10	380	1161
	MHF#2	---	10	3.2E-12	2.1E-10	70	482
	MHF#3	---	10.4	2.2E-12	5.0E-12	2	274
SBH4	MHF#4	---	10.9	1.9E-12	1.1E-10	60	2258
	MHF#5	---	9.7	5.9E-13	8.7E-13	2	1692
	MHF#6	---	9.1	2.2E-12	7.0E-11	30	772
	MHF#7	---	11.5	3.1E-12	2.2E-10	70	406
	HTPF#1	S3.1	28.8	3.8E-12	9.1E-10	240	253
INJ1	HS#2	S1.3	797	2.5E-09	2.2E-07	90	1203
	HS#3	S1.2	831	4.8E-10	2.3E-07	490	314
	HS#4	S3.1	1253	1.2E-07	1.2E-07	1	5606
	HS#5	S3.2	1211	1.2E-08	5.5E-08	5	2452
	HS#8	S1.1	1258	2.8E-10	7.5E-08	270	3703
	HF#1	---	971	2.9E-13	7.5E-10	2550	N/A
	HF#2	---	816	4.2E-13	4.0E-10	950	N/A
	HF#3	---	893	3.8E-13	4.5E-10	1190	N/A
	HF#5	---	1235	1.5E-13	6.1E-11	420	N/A
INJ2	HS#1	S1.3	982	8.3E-11	1.5E-07	1850	560
	HF#6	S1.3	943	4.0E-10	1.7E-09	4	104
	HF#8	---	1501	3.1E-13	1.2E-10	165	362

References

- Amann, F., et al. (2017), The seismo-hydro-mechanical behaviour during deep geothermal reservoir stimulation: open questions tackled in a decameter-scale in-situ stimulation experiment. Solid Earth Discuss., https://doi.org/10.5194/se-2017-79
- Jalali M.R., et al. (2017), Mechanical, hydraulic and seismological behavior of crystalline rock as a response to hydraulic fracturing at the Grimsel Test Site. *51st US Rock Mechanics/Geomechanics Symposium*. American Rock Mechanics Association, 2017.
- Krietsch, H., et al. (2017), Stress measurements in crystalline rock: Comparison of overcoring, hydraulic fracturing and induced seismicity results. *51st US Rock Mechanics/Geomechanics Symposium*. American Rock Mechanics Association, 2017.

SCCER SoE
SWISS COMPETENCE CENTER for ENERGY RESEARCH
SUPPLY of ELECTRICITY

SCCER-SoE Annual Conference 2017

In cooperation with the CTI
Energy
Swiss Competence Centers for Energy Research
Schweizerische Eidgenossenschaft
Confédération suisse
Confederazione Svizzera
Confederaziun svizra
Swiss Confederation
Commission for Technology and Innovation CTI

70 NRP Energy Turnaround
National Research Programme

A matlab package for thermo-hydraulic modeling and fracture stability analysis in fractured reservoirs

Gunnar Jansen , Benoît Valley and Stephen A. Miller
Centre for Hydrogeology and Geothermics - University of Neuchâtel

Motivation

A large fraction of the world's water and energy resources are located in naturally fractured reservoirs within the earth's crust. Understanding the dynamics of such reservoirs in terms of flow, heat transport and fracture stability is crucial to successful application of engineered geothermal systems (also known as enhanced geothermal systems, EGS) for geothermal energy production in the future. The reservoir development characteristics such as permeability creation and induced seismicity largely depend on the traits of pre-existing fractures such as porosity, permeability and orientation within the local stress field. One of the primary driving mechanisms for permeability creation in EGS involves shear failure induced by fluid injection at high pressures.

Methods

We present and validate an implementation of an embedded discrete fracture model (EDFM) for single phase flow and heat transport with additional capabilities to determine fracture stability in fractured reservoirs.

The conceptual idea of the EDFM is the separation of a fractured reservoir into a fracture and a damaged matrix domain. A transfer function accounts for coupling effects between the two domains (Figure 1).

Fracture and matrix domains are computationally independent except for the transfer function. As the fractures are generally very thin and highly permeable compared to the surrounding matrix rock this allows for a lower dimensional representation of fractures.

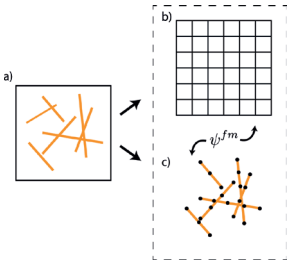

Figure 1: A fractured domain a) is separated in a uniform grid b) and a fracture grid c). The two resulting domains are coupled using the transfer function ψ_{fm}.

Validation on crossing fractures

We compare our solution to a reference solution computed by *COMSOL Multiphysics* which is a widely used finite element package with subsurface flow and transport capabilities. The reference solution is computed on a conforming discrete fracture network were the matrix elements are aligned exactly on the grid with very high resolution.

We evaluate the coupled results of fluid flow and heat transport over 40 years.

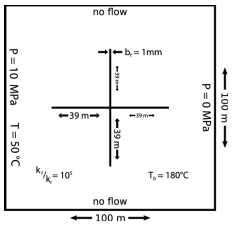

Figure 2: Numerical setup for the initial validation. Incompressible fluids are assumed.

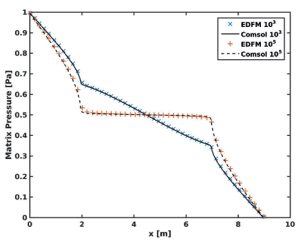

Figure 3: Matrix pressure at y=4.5m. Two permeability contrasts between matrix and fracture are evaluated.

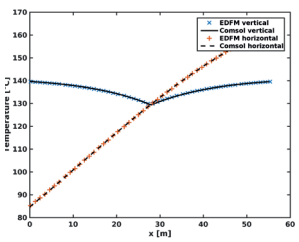

Figure 4: Fracture temperatures through vertical and horizontal fractures after 40 years.

Validation on a complex fracture network

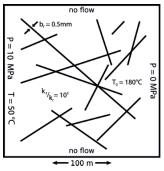

Figure 5: Numerical setup for the validation. Incompressible fluids are assumed.

We evaluate the coupled flow and heat transport on a more complex fracture geometry. The geometry consists of a total of 13 fractures within a square domain.

- Maximum pressure deviations from the reference are below ±5% (NRMSE: 0.35%)
- Maximum temperature deviations from the reference up to 10% (NRMSE: 2.22%)

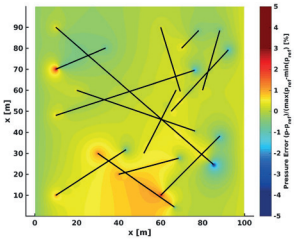

Figure 6: Pressure deviation from reference solution. A region of elevated error is visible in the lower part of the domain. Significant deviations are also visible at some fracture tips.

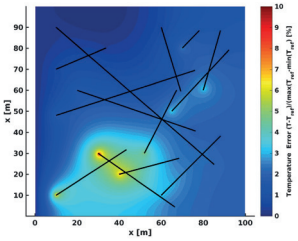

Figure 7: Temperature deviation from the reference solution. The matrix temperatures are generally overestimated compared to the reference.

Fracture stability analysis (FSA)

Fracture slip is likely to occur if the shear stress to effective normal stress ratio equals or exceeds the frictional sliding resistance.

$$T_s = \begin{cases} \frac{\tau}{\sigma_{neff}} < \mu_s & \text{(stable)} \\ \frac{\tau}{\sigma_{neff}} \geq \mu_s & \text{(unstable)} \end{cases}$$

We assume that unstable (sliding) fractures undergo a stepwise change in fracture permeability.

$$k_{fr} = \begin{cases} k_{fr} & \text{if } T_s < \mu_s \\ x \cdot k_{fr} & \text{if } T_s \geq \mu_s \end{cases}$$

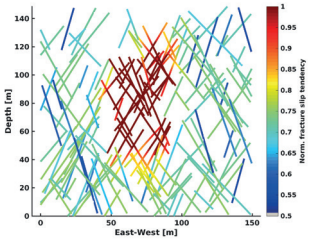

Figure 8: Fracture stability in the reservoir after 10 days of injection. The fracture stability is high with values well below the failure condition (μ = 0.6) in large parts of the reservoir. Stability drastically reduces closer to the injection (red).

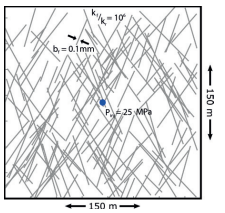

Figure 9: Numerical setup to evaluate the fracture stability. A constant injection pressure of 25 MPa is applied in the borehole (blue circle). On the outer boundaries no-flow boundary condition are assumed.

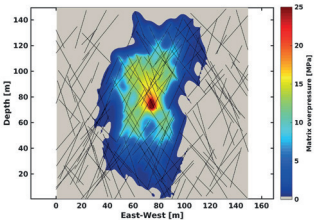

Figure 10: Matrix pressure in the reservoir after 10 days of injection (permeability enhancement factor of *x* = 10). Due to the constant injection pressure, the extend of the high-pressure zone is enlarged.

Conclusion

We validated a fractured reservoir modelling framework implemented in *matlab* which can be used as a standalone simulation package for TH(M) case studies in geothermal reservoirs or as a blue print for the re-implementation of the method e.g. in a high performance computing (HPC) framework. This package will soon be made available to the scientific community as open source.

SCCER SoE
SWISS COMPETENCE CENTER for ENERGY RESEARCH
SUPPLY of ELECTRICITY

SCCER-SoE Annual Conference 2017

In cooperation with the CTI
Energy
Swiss Competence Centers for Energy Research
Schweizerische Eidgenossenschaft
Confédération suisse
Confederazione Svizzera
Confederaziun svizra
Swiss Confederation
Commission for Technology and Innovation CTI

A multi-parametric evaluation of the Wallace-Bott hypothesis in the presence of a fluid source

Maria Kakurina[1], Yves Guglielmi[2], Christophe Nussbaum[1] and Benoit Valley[1]

(1)University of Neuchâtel, CHYN, Neuchâtel, Switzerland, (2)University of California Berkeley, Berkeley, CA, United States, (3)Swisstopo, Wabern, Switzerland

Introduction

Fault slip data inversion methods to estimate the in-situ stress are generally based on the Wallace-Bott hypothesis, stating that the slip on the fault plane occurs in the direction of the maximum resolved shear stress (Wallace 1951, Bott 1959). In this work we focus on validation of the Wallace-Bott hypothesis in the presence of the fluid point source that may induce slip reorientations. A multi-parametric study covering (i) fault geometry such as planar and non-planar faults, (ii) fault orientation, (iii) friction angle, (iv) dilation angles, (v) joint stiffness was performed to understand the effect of each parameter on the misfit angle between the simulated slip vectors and the resolved shear stresses in the presence of the fluid injection.

Methods

- Analytical solution from Bott (1959)
- Numerical solution using the 3D distinct element method (Figure 1)
  - linearly elastic, homogeneous, isotropic, deformable blocks
  - *Coulomb slip* model joint model
  - Active (fracture) and inactive (rock mass) parts of the joint
  - $\sigma_{xx} = 3$ MPa, $\sigma_{yy} = 5$MPa, $\sigma_{zz} = 6$ MPa; $pp = 0.5$ MPa
  - 8 increasing steps of 0.5MPa, starting with a 1 MPa initial pressure
  - Rake of the slipping vectors are compared to the analytical solution

Block		
Mass density, kg/m³	2450	
Bulk modulus, Pa	5.9e9	
Shear modulus, Pa	2.3e9	
Joint	*Active part*	*Inactive part*
Normal stiffness, GPa/m	5.0e11	5.0e11
Shear stiffness, Pa	2.5e11	2.5e11
Friction angle, Pa	22°	40°
Cohesion, Pa	0	1.0e30

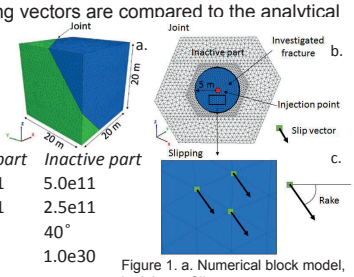

Figure 1. a. Numerical block model, b. Joint, c. Slip vectors

Results

The fluid pressure and shear displacement vectors on the fracture are shown in Figure 2. Increasing fluid pressure decreases the effective normal stress and causes the elastic and subsequent plastic deformation of the model. The perturbation of stress in the vicinity of the fluid source is shown in Figure 3. It can be observed that the stress tensors (cross symbol) is altered by the increasing fluid pressure. After slip occurs, the minimum principal stress is rotating towards the direction perpendicular to the fracture opening due to shear stress release by slip on the fault plane.

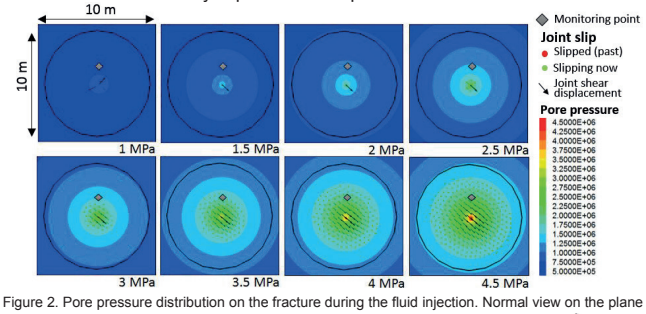

Figure 2. Pore pressure distribution on the fracture during the fluid injection. Normal view on the plane

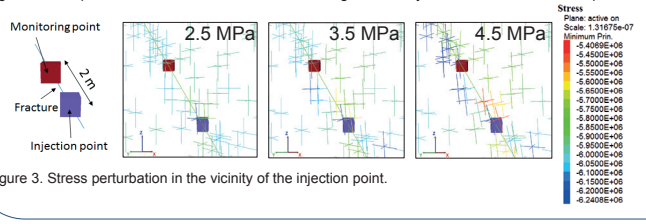

Figure 3. Stress perturbation in the vicinity of the injection point.

Changes in effective stress move the stresses to the joint failure criteria with the fluid pressure increase (Figure 4, left). The numerical result deviates from the analytical solution away from the injection point with increasing fluid pressure and does not exceed 5° (Figure 4, right).

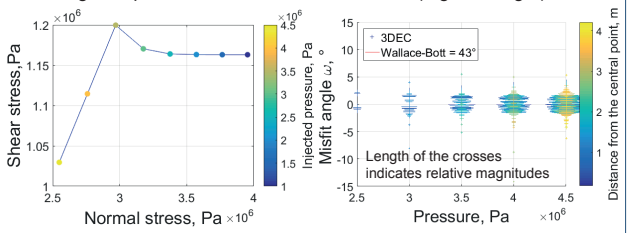

Figure 4. Left-Effect of fluid pressure on sliding condition for the failure envelope. Right - Comparison of the rake computed by 3DEC and by analytical solution on different pressure steps

Sensitivity analysis

The parameters of the model described previously are taken as the reference for this sensitivity study (Figure 5). Therefore, for each model computation, a single parameter is changed from the reference model to address its influence on the results.

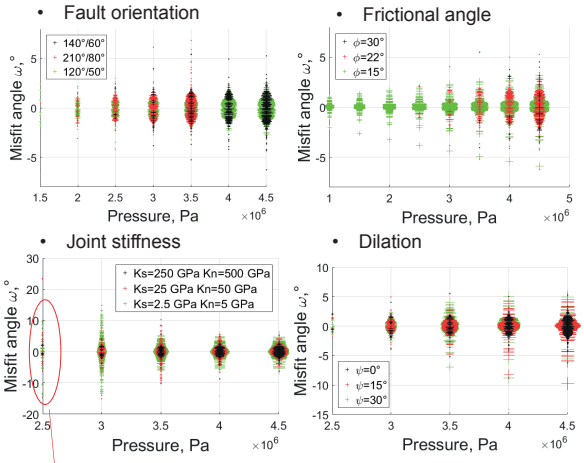

Example of the misfit angle between 3DEC and Wallace-Bott

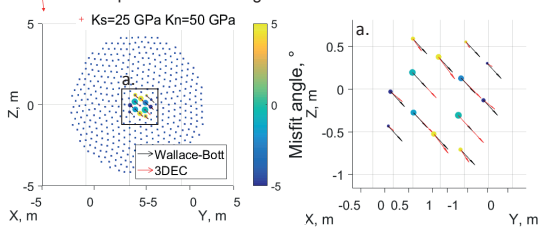

Figure 4. Sensitivity study

Conclusion

- Slip orientation is controlled by the fault geometry and reduced stress tensor
- Fluid injection causes stress perturbation around the injection point
- Generally for a given far-field stress the fluid injection affects the mean misfit angle between the analytical and numerical solutions within the practical threshold (5°).
- Joint stiffness, dilation and friction angle are the key factors influencing the misfit angle. They should be investigated with more details to seek for generalization of the conclusion of this study

References

Bott, M. H. P. (1959). The mechanics of oblique slip faulting. Geological Magazine, 96(02), 109-117.
Wallace, R. E. (1951). Geometry of shearing stress and relation to faulting. The journal of Geology, 59(2), 118-130.

SCCER SoE
SWISS COMPETENCE CENTER for ENERGY RESEARCH
SUPPLY of ELECTRICITY

GEL Geothermal Energy & Geofluids

SCCER-SoE Annual Conference 2017

In cooperation with the CTI
Energy
Swiss Competence Centers for Energy Research
Schweizerische Eidgenossenschaft
Confédération suisse
Confederazione Svizzera
Confederaziun svizra
Swiss Confederation
Commission for Technology and Innovation CTI

Tracer based characterization of the connected fracture volume in the DUG Lab at the Grimsel Test Site

A. Kittilä, K. Evans, M. Jalali, M. Willmann, and M.O. Saar
ETH Zurich

Background

Tracer tests were conducted at the DUG Lab at the Grimsel Test Site (GTS) as part of the ISC experiment (Amann et al. 2017) in order to characterize the connected fracture volume. A total of four tests were conducted, the first two before the hydroshear stimulation program and the second two a month after. Tests 1-3 featured injection into intervals of INJ2 with production from an interval in INJ1, a fracture zone in the AU gallery, and several intervals in PRP observation holes (Tests 2 and 3 only). These tests allow an assessment of changes to flow paths resulting from the stimulations. Test 4 featured injection into two intervals of INJ1 with production from Interval 4 of INJ2, the AU tunnel and the PRP intervals. In this test (and Test 1), novel DNA nanotracer particles were injected with the standard solute dye tracers. The DNA nanotracers provide additional information of the preferential flow paths and the accessible pore volume due to size exclusion.

Materials and Methods

In all four tracer tests, two distinct intervals in the injection hole were injected with two of four available solute dye tracers. The DNA nanotracers (Paunescu et al. 2013) were produced by the company Haelixa.

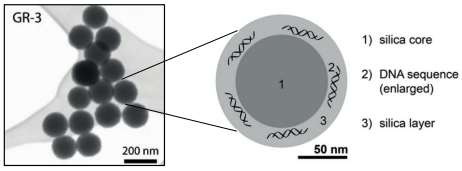

The environmentally friendly DNA-labeled silica particles allow the production of virtually unlimited number of uniquely identifiable tracers exhibiting the same transport properties.

Moment analysis (Shook and Forsmann 2005) was used to determine swept pore volume and flow-storage geometry from the individual recorded tracer concentration histories. First, the concentration histories are normalized to age distribution functions:

$$E(t) = \frac{C(t)\rho q_{\text{out}}}{M_{\text{inj}}},$$

which are used to determine the swept volume:

$$V_p = \frac{m}{M_{\text{inj}}} q_{\text{inj}} \left(\frac{\int_0^\infty tE(t)dt}{\int_0^\infty E(t)dt} - \frac{t_{\text{slug}}}{2} \right).$$

Multi-rate mass transfer (MRMT) model (Haggerty and Gorelick 1995) implemented in **random walk particle tracking (RWPT) method** (Salamon et al. 2006) was applied to characterize the anomalous mass transport. In this approach, the medium is considered to contain overlapping mobile and immobile continua that exchange mass. Immobile zones with different properties can be assigned to account for the different total pore volumes swept by the solute and DNA nanotracers.

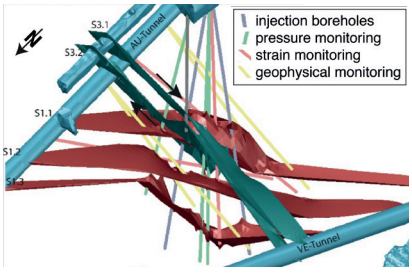

Overview of the DUG Lab (Amann et al. 2017) with two major shear zones S1 and S3, and boreholes. In the tracer tests, only injection (INJ) and pressure monitoring (PRP) boreholes were used.

References

Amann et al. 2017. Solid Earth Discussions, 1-55.
Haggerty and Gorelick 1995. Water Resources Research 31, 2383-2400.
Paunescu et al. 2013. Nature Protocols 8, 2440-2448.
Salamon et al. 2006. Water Resources Research 42, W11417.
Shook and Forsmann 2005. INL/EXT-05-00400, 20 p.

Results

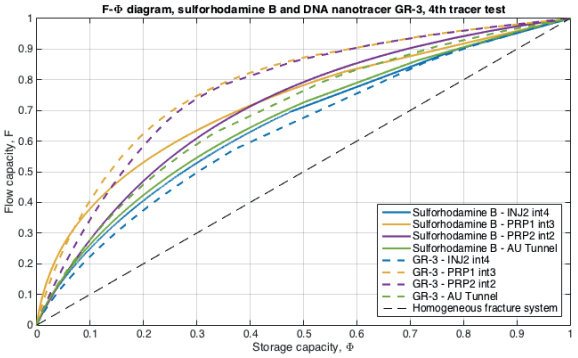

Comparison of flow/storage geometries of solute sulforhodamine B and DNA nanotracer named GR-3. Deviation from the diagonal is a measure of flow path heterogeneity, or channeling. In general, the DNA nanotracers experience more channeling, i.e., smaller pore volumes provide larger fractions of the total flow.

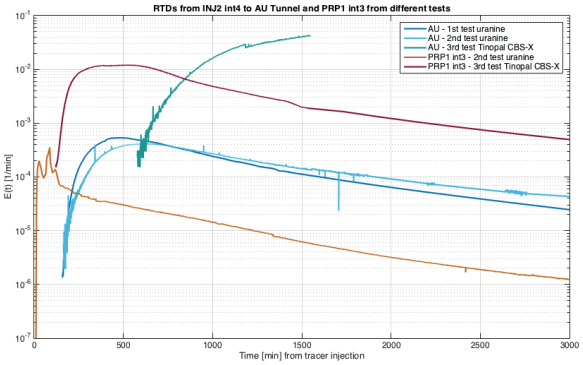

Illustration of tracer signals recorded at the AU Tunnel and PRP1 borehole from Tests 1-3 that all feature injection into Interval 4 of the INJ2 borehole. Test 3 was conducted after the stimulation phase. Stimulation did not directly target either of the structures, but the significant delays in the signals from Test 3 was unexpected. We hypothesize that residual thermal effects from injection of warmer water immediately prior to Test 3 had a larger influence than the stimulation.

The analysis of the anomalous transport with the MRMT model is on-going.

Discussion and Outlook

- The DUG Lab fracture volume was characterized by combining DNA nanotracer particles and solute dye tracers.
- Four tracer tests have been completed, each of which had two separate injections.
- The early termination of Tests 1-3 required undesirable data extrapolation. Future tests should be continued for a longer time.
- The DNA nanotracers arrived invariably earlier than the solutes.
- The results show that the swept volume of the DNA nanotracers is about a tenth of that from the solute tracer for the same injection-production pairs.
- Indications of multiple preferential flow paths are seen in several recorded tracer signals.
- The on-going analysis with the MRMT model will be used to evaluate the interplay between heterogeneous flow field and different mass transfer processes.

In situ characterization of groundwater flow and heat transport in stimulated fractured network using DTS

Maria Klepikova, Bernard Brixel, Reza Jalali, Simon Loew, Florian Amann

ETH Zurich, Geological Institute, Zurich, Switzerland

Objectives

Stimulation and Circulation (ISC) experiment at the Grimsel Test Site is dedicated to study seismo-hydro-mechanical coupled processes relevant for the development of a sustainable heat exchanger in low permeability crystalline rock under controlled conditions. Distributed Temperature Sensing (DTS) technology offers great promise for locating discrete fractures and measuring their hydraulic and heat exchange properties. We use Active - DTS tests and cross-borehole thermal tracer tests to investigate ground water flow and heat transport in fractured media before and after hydraulic stimulation.

Distributed Temperature Sensing at Grimsel Test Site (GTS)

DTS uses the Raman backscatter characteristics of light emitted following a laser pulse into a fiber optic cable to determine the distributed temperature along fiber with a spatial resolution of a few decimeters and temporal resolution of several seconds. At GTS several boreholes were equipped with distributed temperature-sensing optical fibers that are grouted in place.

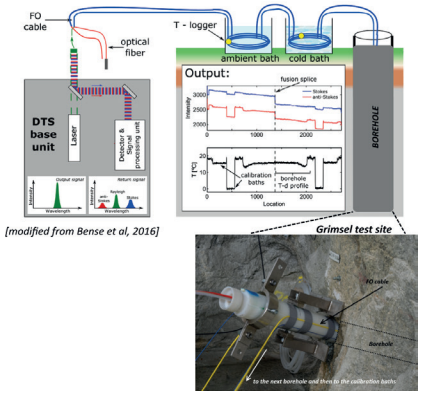

[modified from Bense et al, 2016]

Figure: Schematic of DTS principles based upon Raman backscatter detection. In this cartoon, a fiber-optic cable is deployed in a double-ended setup [1].

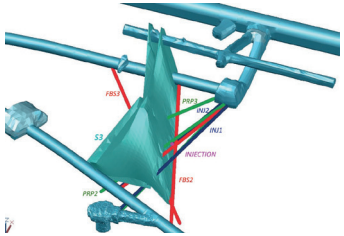

Figure: The boreholes drilled for the ISC experiment. PRP 1-3 and FBS 1-3 boreholes are equipped with DTS FO cables. The S3 shear zone is the target zone for the hydraulic stimulation.

Active-DTS Experiment

In A-DTS, the electrical heating cable [2, 3] or borehole fluid [4, 5] is heated. The temperature response along the FO cable deployed in the middle of the borehole during the heating and subsequent cooling allows:

- In situ determination of rock thermal properties.
- Fracture detection.
- Characterization of fracture inflows.

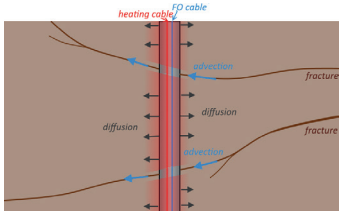

Figure: Schematic of Active-DTS method in a well intersecting two transmissive fractures. Heating- and cooling data can be used to infer thermal properties of the formation as well as groundwater flow.

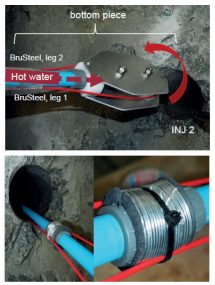

Figure: Measurement setup for A-DTS tests in INJ 1 and INJ 2 boreholes. The bottom-piece and the connection points of the DTS /injection rod. The cable connection points were isolated towards the injection tube with pieces of foam.

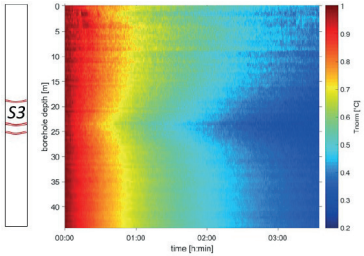

Figure: Normalized FO-DTS data showing relative temperature anomaly from A-DTS test in INJ 2 while INJ 1 was pressurized to 5.5 bar. 1 corresponds to initial temperature anomaly at respective depth, 0 means a full recovery to ambient groundwater temperature. The impact of the cooling inflow at $23.5\ m$ is pronounced. At this depth the S3 shear zone intersects the INJ2 borehole.

Cross-borehole thermal tracer test

A cross-borehole thermal tracer test is analyzed to identify fractures involved in heat transport and to measure thermal breakthrough curves in multiple observation points located at different distances from the injection point. The subsequent analysis of the measured breakthrough curves may provide new insights on flow channeling as well as fracture geometry [6].

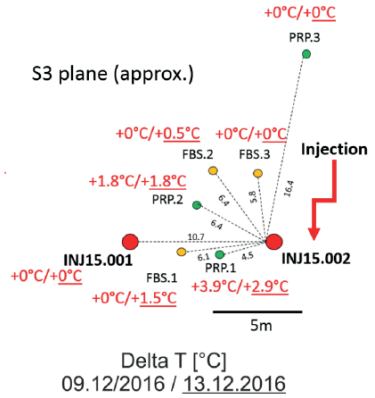

Figure: DTS measurements during the thermal tracer test conducted before the hydraulic stimulation. In-plane view of thermal anomalies measured in observation boreholes 10 and 14 days since the beginning of the heat injection in INJ 2.

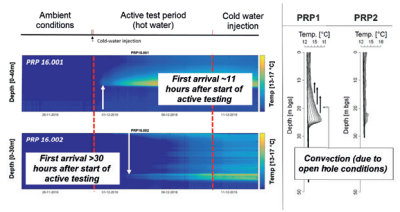

Figure: DTS measurements in PRP 1 and PRP 2 boreholes during the thermal tracer test conducted before the hydraulic stimulation.

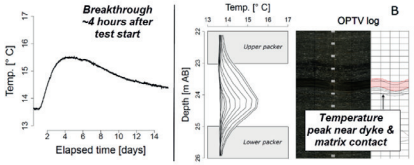

Figure: DTS measurements in PRP 1 borehole during the thermal tracer test conducted after the hydraulic stimulation.

Conduction of tests before and after hydraulic stimulation allows to quantify the effect of hydraulic stimulation on distribution of hydraulic and heat transport properties.

Conclusion

Our study confirms that FO DTS enables investigation of hydrogeological processes with high spatial and temporal resolution. In particularly, DTS monitoring in active mode allows fracture detection and characterization of fracture hydraulic properties similarly to fluid conductivity logs. The advantage of the A-DTS compared to the classical fluid conductivity logging is that

- no salt is added to the system
- measurements are conducted without logging-induced mixing

Cross-borehole heat tracer tests allows to understand heat transport processes in fractured media. Conduction of tests before and after hydraulic stimulation allows to quantify the effect of hydraulic stimulation on heat exchange properties of the media.

References

[1] V. F. Bense, T. Read, and A. Verhoef.
Using distributed temperature sensing to monitor field scale dynamics of ground surface temperature and related substrate heat flux.
Agricultural and Forest Meteorology, 220:207–215, 2016.

[2] T. Read, O. Bour, V. Bense, T. Le Borgne, P. Goderniaux, M.V. Klepikova, R. Hochreutener, N. Lavenant, and V. Boschero.
Characterizing groundwater flow and heat transport in fractured rock using fiber-optic distributed temperature sensing.
Geophysical Research Letters, 40(10):2055–2059, may 2013.

[3] Thomas I. Coleman, Beth L. Parker, Carlos H. Maldaner, and Michael J. Mondanos.
Groundwater flow characterization in a fractured bedrock aquifer using active DTS tests in sealed boreholes.
Journal of Hydrology, 528:449–462, 2015.

[4] T. Read, V. F. Bense, R. Hochreutener, O. Bour, T. Le Borgne, N. Lavenant, and J. S. Selker.
Thermal-plume fibre optic tracking (T-POT) test for flow velocity measurement in groundwater boreholes.
Geoscientific Instrumentation, Methods and Data Systems, 4(2):197–202, 2015.

[5] Andrew T. Leaf, David J. Hart, and Jean M. Bahr.
Active Thermal Tracer Tests for Improved Hydrostratigraphic Characterization.
Ground Water, 50(5):726–735, 2012.

[6] Maria V. Klepikova, Tanguy Le Borgne, Olivier Bour, Marco Dentz, Rebecca Hochreutener, and Nicolas Lavenant.
Heat as a tracer for understanding transport processes in fractured media: Theory and field assessment from multiscale thermal push-pull tracer tests.
Water Resources Research, 52(7):5442–5457, 2016.

Contact Information

- Web: https://sites.google.com/site/klepikovalambert/
- Email: maria.klepikova@erdw.ethz.ch
- Phone: +41 (0)44 633 80 24

How much can we interpret mineral surface area with distributions of minerals and pores ?

Xiang-Zhao Kong[1,*], Jin Ma[1], Duncan Webster[2], Martin O. Saar[1]
[1]Geothermal Energy & Geofluids Group, Department of Earth Sciences, ETH-Zürich, CH-8092, Switzerland (Corresponding Email: xkong@ethz.ch)
[2]SCANCO Medical AG, Fabrikweg 2, CH-8306, Bruettisellen, Switzerland

Introduction

Fluid-rock reactions play an important role in many geo-engineering processes, such as Enhanced Geothermal Systems (EGS) and Carbon Capture, Utilization, and Storage (CCUS). These reactions may change the reservoir permeability dramatically by mineral precipitation and/or dissolution:

- unfavorable reactions can lead to a significant decrease of reservoir productivity/injectivity in EGS and CCUS;
- favorable reactions can lead to a higher heat productivity in EGS or facilitate long-term CO_2 mineral trapping in CCUS.

However, the progress of these reactions depends on individual mineral accessible surface areas that are, in general, poorly constrained for natural geologic samples. In general, reactive surface area is estimated using methods including geometric model, Brunauer–Emmett–Teller (BET) gas absorption method, batch and flow-through experiments, and imaging technologies based on the principle of stereology. In this study, we take the advantages of both BET method and imaging technologies to determine accessible reactive surface areas of individual minerals. These measurements will be later calibrated in future flow-through experiments.

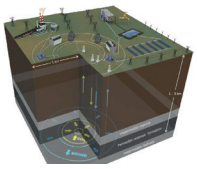

Buscheck, Bielicki, Edmunds, Hao, Sun, Randolph, Saar, Geospheres, 2016

Sample characterization

The rock samples used in this study are sandstones from a depth of 954.6 m from Geothermal well Vydmantai-1, located at the Southeast coast of the Baltic Sea of Lithuania. A thin section microscopy image (Figure 1) indicates an average grain size of 65 μm - 250 μm.

The rock composition (Table 1) was determined using XRF, XRD, and SEM image processing. Chemical formulas of individual minerals were determined by quantitative SEM chemical analysis.

Table 1 Rock composition

Mineral	Average chemical formula	Density g/cm³	XRF+XRD vol.%	SEM vol. %
Quartz (Qtz)	SiO_2	2.62	47.65	45.53
Dolomite (Dol)	$CaMg_{0.77}Fe_{0.23}(CO3)_2$	2.84	12.36	12.22
K-feldspar (Ksp)	$KAlSi_3O_8$	2.56	11.82	9.93
Muscovite (Mu)	$K_{0.85}Na_{0.15}Al_2(AlSi_3O_{10})(OH)_2$	2.82	5.38	4.76
Kaolinite (Kln)	$Al_{1.9}Si_{2.1}O_5(OH)_4$	2.60	0.91	5.64
Ilmenite (Ilm)	$Fe_2Ti_5O_{12}$	4.72	0.23	0.27

The volume fraction of individual minerals calculated from SEM results (Table 1). This promotes the usage of further image analyses for mineral accessible surface area.

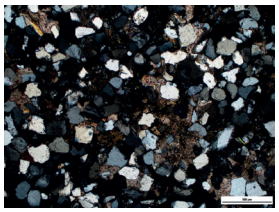

Figure 1 Transmitted light microscopy interference colour image of thin section

Helium gas pycnometry measurements provide a sample porosity of 21.9±0.4%, which agrees well with the estimated porosity of 21.65% from 2D image analyses on the binary image (Figure 2b). Both images agrees well with XRD and XRF

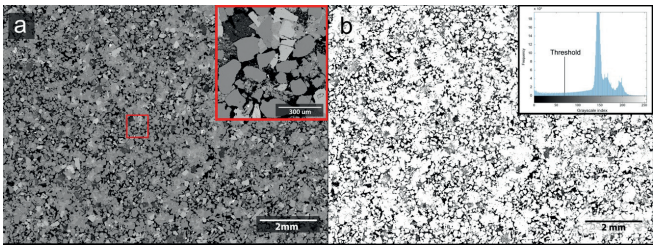

Figure 2 SEM-BSE analysis results: (a) grayscale SEM-BSE image with resolution of 1.2 μm and a x5 zoom-in on the top right, (b) the binary image with black presenting pores and white representing grains. (Inset) grayscale histogram of the SEM-BSE image.

Both SEM-BSE (Figure 2a) and SEM-EDS (Figure 4) images were collected on the same thin section area (11.37mm x 8.34 mm) with pixel resolutions of 1.2 μm and of 2.4 μm, respectively. A binary image (Figure 2b) was converted from the SEM-BSE image, using a threshold of 70, on a scale of 0 to 255 (black to white).

Pore size distribution (PSD)

The pore-size distribution (PSD) (Figure 3) was analyzed using three methods, including mercury (Hg) intrusion porosimetry, analyses of SEM-BSE (1.2 μm), and 3D CT (19.5 μm) images. In general, all measurements agree well with each other. The discrepancies are very likely introduced by the difference in measuring principles (pore throat size during mercury injection methods and pore size during image processing). In 3D CT analysis, due to limited resolution, most pores have been filtered out and only ~16% pores (relatively large) remain 'visible'. However, there is still a good match between results for the 2D and 3D image analyses. This provides a positive validation for the stereological method used in this study.

Figure 3 Pore size measured using porosimetry, SEM image analysis (Figure 2b) and 3D micro-CT analysis.

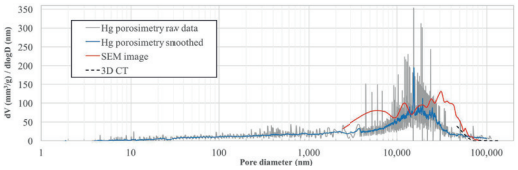

Reactive surface area analysis

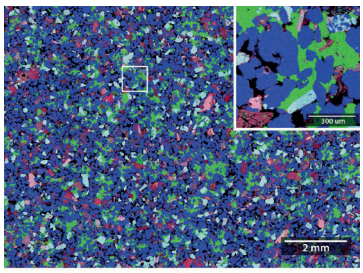

Figure 4 Mineral distribution on the SEM-EDS image (2.4 μm resolution).

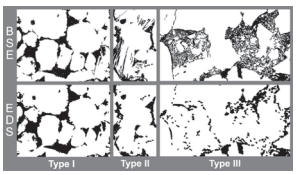

Figure 5 Comparison of the binary images of SEM-BSE (top) and SEM-EDS (bottom). In mineral fraction and surface area analyses, minerals were classified into 3 groups: (I) minerals with fully filled grains, such as quartz, dolomite, K-feldspar, and ilmenite; (II) minerals with partially filled grains, such as muscovite; (III) minerals with poorly filled grains, such as Kaolinite. To minimize the differences between BSE and EDS images, different corrections are applied to different groups (type) of minerals.

To minimize the resolution mismatch between the SEM-BSE and the SEM-EDS images, minerals are grouped into 3 different types (Figure 5). Then corrections for each group were applied to reduce the relative difference of the perimeter density from 40.0% to 2.9%.

Mass-specific surface area (SSA) of whole rock samples was measured by the BET method with nitrogen as the adsorption gas at a temperature of 77.3 K. A bulk mass-SSA = 1.447 m^2/g was obtained using a 5-point method with a correlation coefficient of R^2=0.99995.

Perimeter density (m/m^2), *i.e.*, the ratio between solid perimeter and solid area, was first calculated using the SEM-BSE binary image (Figure 2b). Based on the principle of stereology (Weibel, 1969), mass-SSA (m^2/g) was then the product of a bias correction factor of $4/\pi$, the reciprocal of bulk rock density that is measured to be 2.11 g/cm^3, and the perimeter density. The stereological analyses on both the SEM-BSE image (Figure 2b) and the SEM-EDS image (corrected) yield mass-SSA values of 0.031 m^2/g and 0.032 m^2/g, respectively.

Roughness correction was also applied to individual minerals such that a good match to the BET measurements of the sample SSA can be achieved. Table 2 shows the BET literature values for pure individual minerals, accessible surface areas and their fractions before and after the corrections with different correction factors listed in Table 2. Compared to literature values, our SSA values for individual minerals are reasonable. The bulk SSA, i.e., the overall accessible SSA of all minerals, is then calculated to be 1.441 m^2/g, i.e., close to the bulk BET measurement (1.447 m^2/g).

	Pore	Qtz	Dol	Ksp	Mu	Kln	Ilm	Total
EDS Area Fraction (AF) (%)	21.64	44.82	12.03	9.77	4.88	6.29	0.27	99.7
EDS PD (m/m^2) of mineral grains		63003.3	64049.7	60724.7	102063.2	196802.0	147541.4	
Accessible EDS PD (m/m^2)		18382.6	1605.5	2181	1767.8	6875.4	242.1	31054.5
Correction due to resolution difference between BSE and EDS images (perimeter density (PD) obtained from BSE image: 51567.3 m/m^2)								
Correction factor for EDS AF		1.02^I	1.02^I	1.02^I	0.98^{II}	0.9^{III}	1.02^I	
Corrected EDS AF (%)	21.65	45.53	12.22	9.93	4.76	5.64	0.27	100
Correction factor for EDS PD		1.3^I	1.3^I	1.3^I	1.94^{II}	2.98^{III}	1.3^I	
Corrected accessible EDS PD (m/m^2)		23897.4	2087.2	2835.3	3429.5	20488.8	314.7	53052.9
Roughness correction based on literature BET SSA of pure mineral grains and later calibrated to measured bulk BET SSA: 1.447 m^2/g)								
Accessible mass-SSA (m^2/g) calculated from corrected EDS PD		0.0144	0.0013	0.0017	0.0021	0.0124	0.0002	0.032
Accessible SSA fraction (%)		45.05	3.93	5.34	6.47	38.62	0.59	
Mass-SSA (m^2/g) of mineral grains calculated from corrected EDS PD		0.04	0.037	0.039	0.089	0.230	0.052	
Typical literature BET mass-SSA (m^2/g)		0.02-0.55	0.07-1.96	0.08-0.25	0.66-5.53	13.2-78.0	n.a.	
Correction factor for calculated mass-SSA		5	50	5	50	100	25	
Corrected mass-SSA (m^2/g) of mineral grains		0.20	1.87	0.19	4.47	23.04	1.29	
Corrected accessible mass-SSA (m^2/g)		0.07	0.06	0.01	0.06	1.24	0.005	1.441
Accessible mass-SSA fraction (%)		5.00	4.37	0.59	3.59	85.79	0.66	

Table 2 Various corrections for mineral area fractions (AF), perimeter density (PD) and specific surface areas (SSA) based on SEM-BSE image and BET values from literatures. Superscripts I, II, and III represent the three types of minerals in Figure 5.

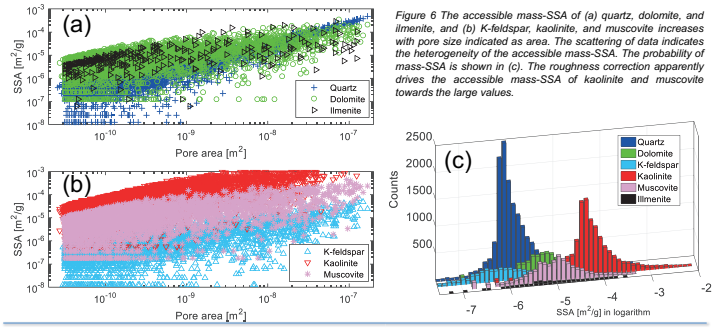

Figure 6 The accessible mass-SSA of (a) quartz, dolomite, and ilmenite, and (b) K-feldspar, kaolinite, and muscovite increases with pore size indicated as area. The scattering of data indicates the heterogeneity of the accessible mass-SSA. The probability of mass-SSA is shown in (c). The roughness correction apparently drives the accessible mass-SSA of kaolinite and muscovite towards the large values.

Conclusions

We have quantified porosity and pore-size distribution (PSD) of rock samples, using a Helium gas pycnometer and Hg porosimetry, respectively. Rock compositions are determined by a combination of XRF, XRD, and SEM-EDS, which are later geometrically mapped onto 2D images derived from SEM-BSE. The stereological method used in this study is validated through comparisons of mineral volume fraction, porosity, and PSD results from image processing and laboratory measurements. Normalization of stereological SSA to BET measurements yields roughness corrections of individual minerals. Due to the computational expensive of 3D micro-CT analysis, 3D reactive surface area analysis is still on-going and will be presented in our peer-review paper.

Acknowledgements

This work is supported by an European project, entitled "Demonstration of soft stimulation treatments of geothermal reservoirs project" (DESTRESS), funded by European Union's Horizon 2020 research and innovation program under the grant agreement No.691728. The rock sample is provided by Geoterma, a Lithuanian geothermal energy company. The 3D micro-CT analysis was performed by Dr. Duncan Webster at SCANCO Medical AG, Zurich, Switzerland. The Geothermal Energy & Geofluids (GEG) group is endowed by the Werner Siemens Foundation, which is hereby gratefully acknowledge. The GEG group is also a research partner of SCCER-SoE, Switzerland.

SCCER SoE
SWISS COMPETENCE CENTER for ENERGY RESEARCH
SUPPLY of ELECTRICITY

SCCER-SoE Annual Conference 2017

In cooperation with the CTI
Energy
Swiss Competence Centers for Energy Research
Schweizerische Eidgenossenschaft
Confédération suisse
Confederazione Svizzera
Confederaziun svizra
Swiss Confederation
Commission for Technology and Innovation CTI

Geological characterization and in-situ stress state of the ISC experimental volume

H. Krietsch, V. Gischig, F. Amann, J. Doetsch, M.R. Jalali, B. Valley

Motivation

The In-Situ Stimulation and Circulation (ISC) experiment has recently been carried out at the Grimsel Test Site (Amann et al., 2017). It includes **six hydro-shearing** and **six hydraulic fracturing** experiments. A precise geological model and detailed knowledge of the in-situ stress state is crucial for the analysis and interpretation of the hydromechanical response of the experimental volume to high-pressure fluid injection. For this purpose an extensive geological characterization combining tunnel-mapping, core- and geophysical borehole logging (OPTV, ATV, FWS) was conducted, in combination with detailed geophysical surveys (i.e. GPR and seismic tomography). Additionally, a comprehensive stress measurement campaign, including overcoring (USBM & CSIRO HI) and hydraulic fracturing was carried out (Gischig et al., 2017, Krietsch et al., 2017).

Geological Model

The precise locations and orientations of shear zones and fractures were mapped using geophysical borehole and core logs. In total five shear zones are identified: three S1 (strike N52°E) and two S3 (strike N93°E) shear zones. The three S1 shear zone are characterized by an increase in foliation intensity. The two S3 shear zones are localized in one metabasic dyke, each, and separated by 2.5 m. Additionally, information about fracture density are gathered. As the boreholes approach the shear zones, the fracture density increases from 0-3 frac/m (host rock) to 14-22 frac/m.

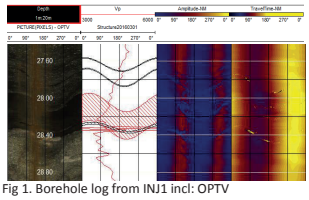

Fig 1. Borehole log from INJ1 incl: OPTV FWS and ATV

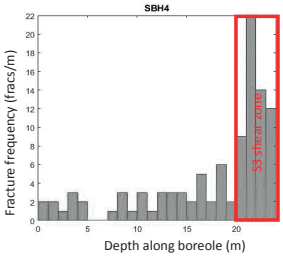

Fig 2. Fracture density along SBH4 with increase fracture density towards the shear zone

Tu build a geological model, geological observations are combined with geophysical surveys. The combination of geological mapping and seismic tomography revealed a highly fragmented zone between the two S3 shear zones that correlates with a drop in P-wave velocity. A dextral shear sense along the S3 shear zone was determined from mapping of S1 shear zones and GPR.

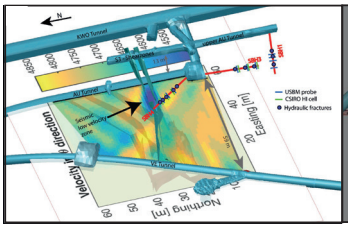

Fig 3. Seismic tomography combined with geological model. Highly fractured zone visitble as low p-wave-velocity zone. Stress measurement locations are indicted, too.

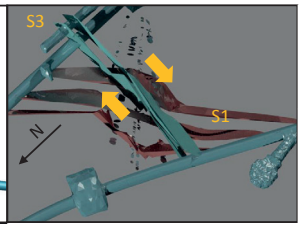

Fig 4. Three S1-orientated shear zones (red) and two S3-orientated shear zones are shown with fractures along PRP and INJ boreholes are shown, and shear sense of the S3-shear zone.

Stress measurements

Two stress field solutions were found : one for the 'far-field' and one close to the shear-zone. The orientations obtained from USBM, CSIRO-HI and HF are consistent for each tensor.

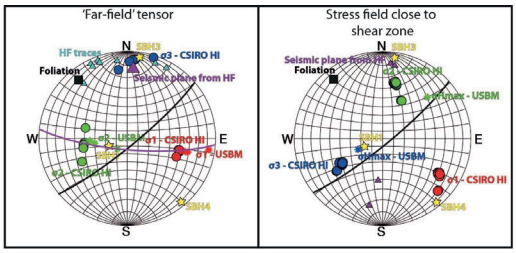

Fig 5. Final orientations of the stress tensors. Circles: CSIRO HI results; Small stars: USBM results; Yellow star: boreholes; Triangle: HF results; Half-circles: foliation plane (black), seismic plane (purple).

The magnitudes for the 'far-field'-tensor range from 13.1 to 14.4 MPa for σ_1, 9.2 to 10.2 MPa for σ_2, and 8.6 to 9.7 MPa for σ_3. A drop in principal stress magnitudes was observed, as the measurements approached the shear zones.

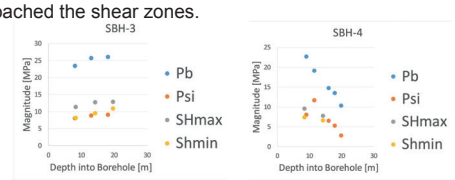

Fig 6. Stress magnitudes for SBH3 and SBH4. SBH3 measures the ‚far-field' and SBH4 the stress drop as it approaches the shear zone.

Combination of geology and stress field

Based on the 'far-field' tensor the slip and dilation tendencies of all mapped geological structures were calculated. S1 shear zones have the highest slip tendencies, and S3 shear zones the highest dilation tendencies.

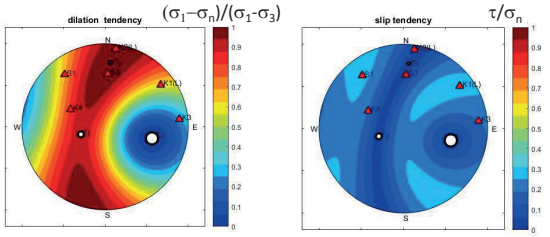

Fig 7. Dilation and slip tendency based on ‚far-field' tensor correlated with mapped geological structures.

ATV logs conducted after hydroshearing experiment of an S1 parallel fracture indicate shear dislocation along stimulated structure. The offset can be quantified.

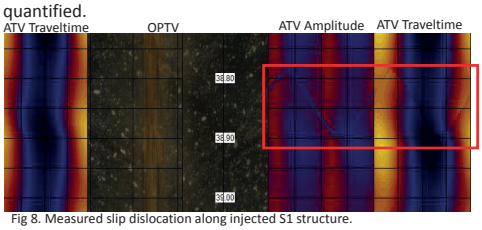

Fig 8. Measured slip dislocation along injected S1 structure.

References

Amann, F., et al. (2017), The seismo-hydro-mechanical behaviour during deep geothermal reservoir stimulation: open questions tackled in a decameter-scale in-situ stimulation experiment. Solid Earth Discuss., https://doi.org/10.5194/se-2017-79

Gischig, V., et al. (2017), On the link between stress field and small-scale hydraulic fracture growth in anisotropic rock derived from microseismicity. Solid Earth Discuss., https://doi.org/10.5194/se-2017-78

Krietsch, H., et al. (2017), Stress measurements in crystalline rock: Comparison of overcoring, hydraulic fracturing and induced seismicity results. *51st US Rock Mechanics/Geomechanics Symposium*. American Rock Mechanics Association, 2017.

SCCER SoE
SWISS COMPETENCE CENTER for ENERGY RESEARCH
SUPPLY of ELECTRICITY

SCCER-SoE Annual Conference 2017

In cooperation with the CTI
Energy
Swiss Competence Centers for Energy Research
Schweizerische Eidgenossenschaft
Confédération suisse
Confederazione Svizzera
Confederaziun svizra
Swiss Confederation
Commission for Technology and Innovation CTI

Deformation and tilt measurements during the ISC experiment at the Grimsel Test Site

H. Krietsch, V. Gischig, B. Valley, F. Amann

Motivation

A decameter scale stimulation experiment, including six hydraulic shearing (HS) and six hydraulic fracturing (HF) experiments, has recently been conducted at the Grimsel Test Site. One aim was the quantification of the spatial mechanical response during high pressure fluid injections into a pre-existing fracture network and intact rock mass. Multiple Fibre Bragg-Grating (FBG) sensors, distributed fibre optics strain systems (DBS) and tiltmeters were installed to monitor the deformations. In this contribution we present exemplary results from HS and HF experiments.

Sensors

A total of 60 FBG sensors were distributed in three differently oriented boreholes, covering intact rock and various fractures. The sensors average the strain over a 1 m baselength, and have a resolution of 0.1 µstrain and accuracy of 1 µstrain. Additionally, two DBS chains with a resolution of 1 µstrain and accuracy of 10 µstrain, covering three boreholes, each, were installed. At the tunnel west of the experiment, three tiltmeters were installed measuring the deviation from horizontal in two axes with a sensitivity of 0.1 µradians.

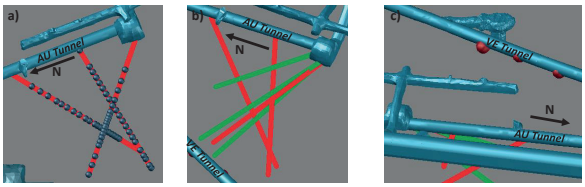

Figure 1. Sensor locations in the test volume: a) 20 FBG-sensors per borehole, b) FBS (red) and PRP Boreholes (green) with one loop per group, c) Position of three tiltmeters in VE-tunnel west of volume.

FBG strain measurements

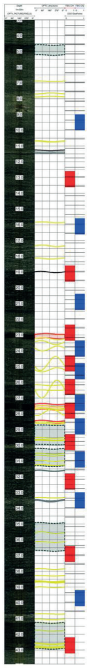

Figure 2. Exemplary borehole design for FBS1-borehole.

Depending on their position within the boreholes, the FBG sensors show different behaviour during the fluid injection. The magnitude of the recorded strain depends on the distance between sensor and injection interval, and whether the sensor covers a fracture or not. For the stimulation experiment HS1 (injection into S1 shear zone) the recorded strains in FBS3 may indicate a dextral shearing of the S1 shear zone. This may be interpreted from the tensional behaviour in the upper half of the borehole and the compressional behaviour at the lower part.

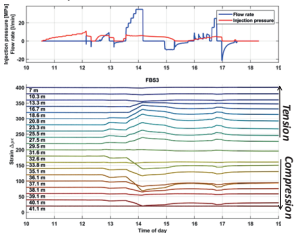

Figure 3. Transient strain signals in FBS3 during HS1 correlated with the injection flow rate and pressure

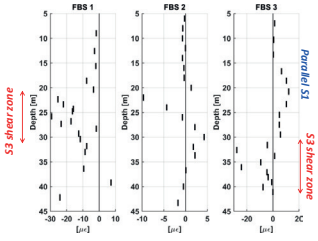

Figure 4. Maximum recorded strains during HS1 experiment. The strain signals indicate different behaviour depending on borehole orientation and sensor locations.

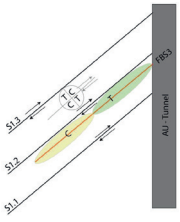

Figure 5. Schematic interpretation of the HS1 experiment, with indicated shear sense along S1 shear zones.

DBS strain measurements

Compared to the FBG sensors, the DBS have a resolution too low to precisely monitor the deformation due to the stimulations. In each borehole, one leg was packed (i.e. distinct base length of 0.6 m) and one leg was bare. The measurements indicated that the packed leg is more accurate than the bare one, but still of lower quality than the FBG recordings. For the description of the spatial mechanical response during the stimulation, the DBS is used in a qualitative way. In the PRP boreholes the movement of the packer due to an increase in interval pressure is visible in the strain data. During HF8 the hydrofrac propagated through the resin (yellow) above interval 1 in PRP2, which can be seen in the DBS.

.

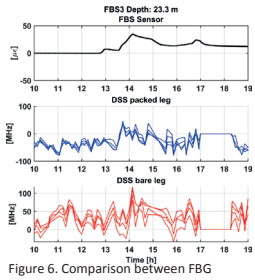

Figure 6. Comparison between FBG sensors, packed and bare leg DBS measurements in FBS3. Data represent strain at specific point over time.

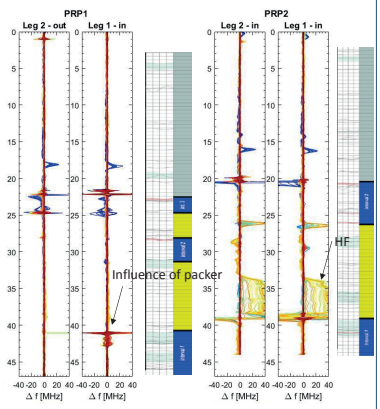

Figure 7. Distributed strain signals in PRP boreholes. Strong influence of packer movement can be observed. Above interval 1 in PRP2 a hydrofrac propagated through the resin.

Tilt measurements

Tilt measurements are as additional constrain for the orientation of stimulated shear zone. The tilt signals need to be corrected for the tunnel free surface effects with help of numerical modeling .

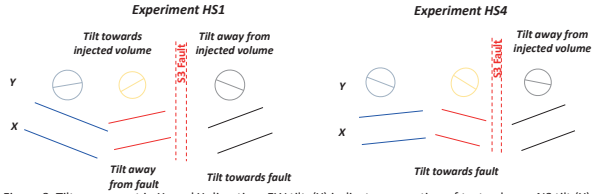

Figure 8. Tilt movement in X- and Y-direction. EW tilt (Y) indicates expantion of test volume. NS tilt (X), is sensitive to shear zone orientation and injection location. HS1 and HS4 indicate different behaviour in X-tilt, due to different orienation of shear zone, and different location of injection interval.

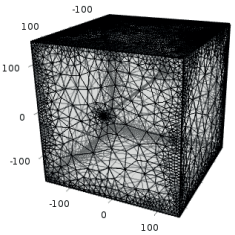

Figure 9. Geometry of tilt model. Normal opening of penny-shaped fractur with different orientations.

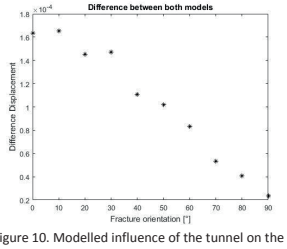

Figure 10. Modelled influence of the tunnel on the tilt-field. Difference displacement represents ratio tunnel/rock mass displacement.

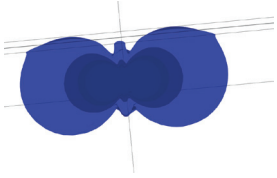

Figure 11. Displacement field around the opening fracture

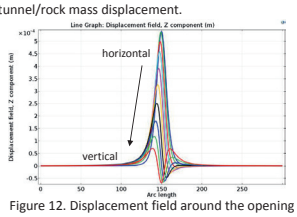

Figure 12. Displacement field around the opening fracture

SCCER SoE
SWISS COMPETENCE CENTER for ENERGY RESEARCH
SUPPLY of ELECTRICITY

SCCER-SoE Annual Conference 2017

In cooperation with the CTI
Energy
Swiss Competence Centers for Energy Research
Schweizerische Eidgenossenschaft
Confédération suisse
Confederazione Svizzera
Confederaziun svizra
Swiss Confederation
Commission for Technology and Innovation CTI

Core-scale reactive transport modelling of injection of CO_2-charged brine into natural sandstone

Jin Ma, Xiang-Zhao Kong, Martin O. Saar*

Geothermal Energy and Geofluids, Institute of Geophysics, ETH Zurich, Switzerland
** Email: jin.ma@erdw.ethz.ch*

Introduction

Fluid-rock reaction is an important process involved in many geological and geo-engineering systems such as chemical stimulation of enhanced geothermal systems (EGS) (Potier et al., 2009) and carbon capture, utilization, and storage (CCUS) (Guas, 2010; Xu et al., 2003). These reactions lead to mineral dissolution and precipitation which may cause changes of reservoir porosity and permeability (Cai et al., 2009; Nogues et al., 2013). Due to the complexity of coupled fluid flow and fluid-rock reactions in heterogeneous porous media, it is challenging to predict long-term operation performance of geothermal reservoirs.

Geochemical transport modelling is well recognized as a powerful approach to probe the physical and chemical evolution of subsurface systems (Beckingham et al., 2016). In this study, a 1D core-scale reactive transport model is developed to simulate the injection of CO_2-charged brine into a natural sandstone core. We present the simulation results using calculated ion concentrations to interpret mineral dissolution/precipitation reactions in a multi-mineral system.

Model description

We employed PFLOTRAN to perform a 1D core-scale reactive transport simulations at an outlet pressure of 10 MPa and a temperature of 40 ℃. We modelled an injection of CO_2-rich brine at a constant volumetric flow rate of 2 ml/min into a cylindrical sandstone specimen with a length of 3.9 cm and a cross section area of 5.29 cm^2 as shown in Figure 1. The NaCl concentration of the injected fluid is 1 mol/l, and 0.8 mol/l CO_2(aq) was dissolved into it to reach 80% of CO_2 solubility at such simulation conditions.

The rock properties in this model follow a sandstone sample from the geothermal reservoir, Vydmantai (954.6 m deep), Lithuania. Its porosity is measured to be 0.22 using He pycnometer and permeability 300 mD using flow-through experiments. The sandstone composition is listed in Table 1. Other parameters, such as mineral volume fraction and reactive surface area, take the results from analyse of SEM-EDS image (Figure 2). Mineral reaction rate constants are taken from Palandri et al. (2004).

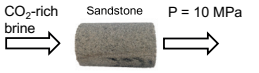

Fig.1 Sketch of the model with constant flow rate at the inlet and constant pressure at the outlet.

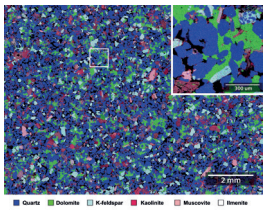

Fig.2 Mineral distribution of the SEM-EDS image with a resolution of 2.4 μm.

Table 1 Mineral system of the rock sample used in the model

Mineral	Formula	Volume fraction (%)	Reactive surface area (cm^2/cm^3)	Rate constant ($mol/cm^2/s$)
Quartz	SiO_2	46.0	1521.4	1.0×10^{-17}
Dolomite	$CaMg(CO_3)_2$	12.0	1328.7	3.0×10^{-8}
K-feldspar	$KAlSi_3O_8$	10.0	180.5	1.0×10^{-12}
Muscovite	$KAl_3Si_3O_{10}(OH)_2$	5.0	1310.0	1.0×10^{-16}
Kaolinite	$Al_2Si_2O_5(OH)_4$	5.0	26087.2	5.0×10^{-16}
Ilmenite	$FeTiO_3$	0.3	100.2	4.5×10^{-13}

Results and discussion

In the following, we only show the concentration of Ca++, because Ca++ and Mg++ only exists in dolomite with a mole ratio of 1:1. Figure 3 shows major ion concentrations at PV=0.53 and PV=793. Concentration of Na+ does not change much during the whole simulation. The simulation results show that when the volume of the injected fluid is less than one total pore volume (PV) of the core, ion concentrations clearly indicate a diffusion-controlled reaction front from 12 mm to 24 mm. At PV=0.53, compared to other cation (K+, Fe++, Al+++, and SiO_2(aq)) concentrations, Ca++ concentration is not affected by the dilation (mixing) at the inlet because of relatively high reaction rate of dolomite. When the injection volume of fluid is more than one pore volume (PV>1), a sharp concentration front is developed due to depletion of minerals, in particular for dolomite. This concentration front is migrating towards the outlet with a speed of 0.0174 mm/PV. Figure 3 shows a typical front pattern at PV=793 where Ca++ concentration is nearly zero from the inlet to the front, followed by a dramatic increment after the front.

Figure 4 shows the saturation index (SI) and the relative change of volume fractions of 5 major minerals in the system at both PV = 0.53 and PV = 793. When PV<1, volume fraction of most minerals do not change, except dolomite due to its high reactivity. The SI profiles indicate a potential dissolution of K-feldspar and a potential precipitation of kaolinite. When PV >1, similar to the concentration profiles, a sharp front is formed at the reaction front. Behind the front, all major minerals stay under-saturated, except for quartz which is closed to equilibrium. At the reaction front, muscovite and kaolinite quickly reach over-saturation but then are back to the equilibrium vicinity. Dissolution of K-feldspar and precipitation of kaolinite along the whole core is suggested.

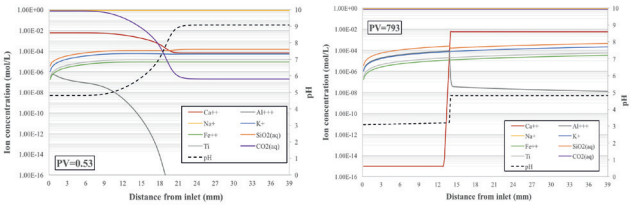

Fig.3 Ion concentrations (mol/L) and pH profiles at injection volumes of PV=0.53 and PV=793.

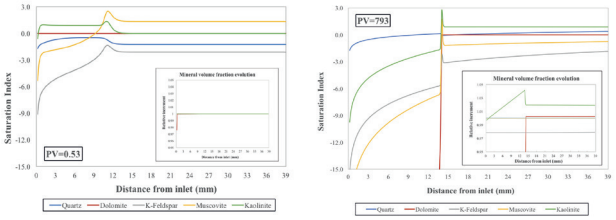

Fig.3 Saturation index (SI) and volume fraction relative change of minerals at injection volumes of (left) PV=0.53 and (right) PV=793.

Acknowledgement

The project is funded by the European Union's Horizon 2020, "DESTRESS" under grant No. 691728.

DESTRESS
GEO Geothermal Energy & Geofluids
ETH Eidgenössische Technische Hochschule Zürich Swiss Federal Institute of Technology Zurich

SCCER SoE
SWISS COMPETENCE CENTER for ENERGY RESEARCH
SUPPLY of ELECTRICITY

SCCER-SoE Annual Conference 2017

In cooperation with the CTI
Energy
Swiss Competence Centers for Energy Research
Schweizerische Eidgenossenschaft
Confédération suisse
Confederazione Svizzera
Confederaziun svizra
Swiss Confederation
Commission for Technology and Innovation CTI

Mixed finite element method for recovering stress and displacement fields

Morteza Nejati, Thomas Driesner
SCCER-SoE, ETH Zurich, Switzerland

Introduction

Stresses and displacements computed directly from the finite element solution of geomechanical problems can be extremely inaccurate when using low order finite elements such as two-noded line element, three-noded triangular element, and four-noded tetrahedral element. These elements are extremely efficient in terms of computation cost, and therefore their use in large geomechanical models is of interest. Stress and displacement recovery methods are designed to improve the accuracy of low order elements for two main reasons: (i) To obtain better estimates of the stress and displacement throughout the domain, and (ii) To provide a benchmark for discretization error estimation which is useful for efficient mesh generation and mesh adaptivity. Previous methods solely focus on stress recovery and are based on polynomial choices outside the ones provided from finite element shape functions. Recovery by equilibrium in patches [1], recovery by compatibility in patches [2], and recovery by enhanced equilibrium in patches [3] are examples of these methods. In this research, a new method called recovery by enhanced compatibility and equilibrium is proposed, which is able to recover displacements as well as stresses, and it only uses the polynomials available from isoparametric element types to enhance the accuracy of the field variables.

Methodology

The two main variational theorems in the theory of elasticity are principle of minimum potential energy, and principle of minimum complementary energy. Minimum potential energy is based of a functional of displacement, where compatibility conditions are satisfied as priori by assuming a continuous displacement over the entire domain and permitted variation of displacement which satisfies the prescribed displacement boundary conditions. This variational equation gives the equilibrium equations. Minimum potential of complementary energy is a functional of stresses, where equilibrium condition is satisfied as priori by assuming equilibrated stresses with body forces and permitted variation of stresses. This variational equation is equivalent to the compatibility of displacements. In these two principles, one of equilibrium or comparability is assumed over the domain, while the other condition is satisfied by the variational equation. Reissner [4] defined a variation theorem in which neither compatibility nor equilibrium is assumed as priori, whereby both equilibrium and comparability are outcomes of the variational equation. This mixed variational theorem does not favor equilibrium over compatability or vise versa, and permits simultaneous use of an assumed stress field and an assumed displacement field.

Let σ_{ij} and u_i be the components of the assumed stresses and displacements, respectively. The Reissner functional π_R is defined in terms of assumed independent stresses and displacements as:

$$\pi_R = \int_\Omega \left(\sigma_{ij}u_{i,j} - \frac{1}{2}\sigma_{ij}S_{ijkl}\sigma_{kl} - F_i u_i\right)\mathrm{d}\Omega - \int_{\Gamma_T} \bar{T}_i u_i \,\mathrm{d}\Gamma - \int_{\Gamma_u} (u_i - \bar{u}_i)T_i \,\mathrm{d}\Gamma \quad (1)$$

Here S_{ijkl} denotes the components of the fourth-order elasticity matrix, F_i is the body force component, Ω is the domain of interest, and $\bar{T}_i$ and $\bar{u}_i$ are the traction and displacement boundary conditions applied along Γ_T and Γ_u. After the finite element solution with low order elements is performed, the displacements are obtained and can be used as the boundary values for single or a patch of elements to solve for more accurate stresses and displacements using the mixed finite element.
Let us assume that $T_i = \bar{T}_i$ on Γ_T The variation of the functional in Eq. (1) with respect to displacement and stress gives:

$$\begin{aligned} &\int_\Omega \delta u_i(\sigma_{ij,j} + F_i)\,\mathrm{d}\Omega = 0 \\ &\int_\Omega \delta\sigma_{ij}(u_{i,j} - S_{ijkl}\sigma_{kl})\,\mathrm{d}\Omega + \int_{\Gamma_u} \delta T_i(\bar{u}_i - u_i)\,\mathrm{d}\Gamma = 0 \end{aligned} \quad (2)$$

By simultaneously solving these two equations for the displacement and stress, highly accurate recovered fields can be obtained.

Results and discussion

Figure 1 compares recovered values against the directly calculated ones as well as the exact values for a one-dimensional model. Figure 2 also shows how the order of convergence increases by using different orders of polynomials for the recovered estimates. These result show that the proposed method is highly efficient in recovering FE values with low accuracy. This is in particular important for efficiently modeling large thermo-hydro-mechanical systems with low-order elements.

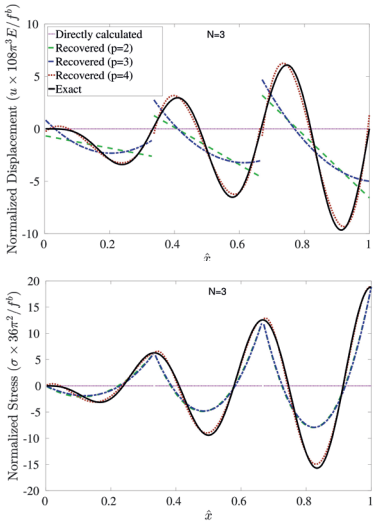

Fig 1. The comparison of directly calculated FE stress and displacement using three elements with the recovered ones and the exact solutions for the 1D problem which is subjected to $F^b = f^b\hat{x}\sin(6\pi\hat{x})$ and fixed at two ends. The recovered values are obtained using stress polynomials of order p and displacement polynomial of order q=p-1 for each individual element.

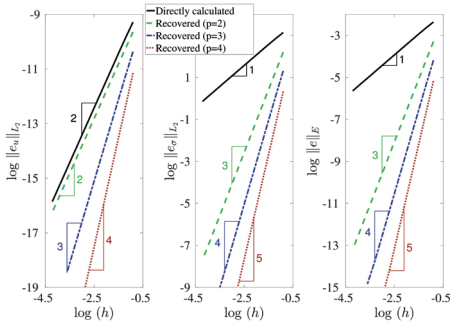

Fig 2. The convergence rate of displacement, stress and energy error estimates by using the proposed approach with polynomials of order p for stress, and q=p-1 for displacement for a one-dimensional problem.

References

[1] Boroomand, B., Zienkiewicz, O. C., 1997. Recovery by equilibrium in patches (REP). International Journal for Numerical Methods in Engineering 164, 137–164.
[2] Ubertini, F., 2004. Patch recovery based on complementary energy. International Journal for Numerical Methods in Engineering 59 (11), 1501–1538.
[3] Payen, D. J., Bathe, K.-J., 2012. A stress improvement procedure. Computers and Structures 112-113, 311–326.
[4] Reissner, E., 1950. On a variational theorem in elasticity. Journal of Mathematics and Physics 29, 90-95.

SCCER SoE
SWISS COMPETENCE CENTER for ENERGY RESEARCH
SUPPLY of ELECTRICITY

SCCER-SoE Annual Conference 2017

In cooperation with the CTI
Energy
Swiss Competence Centers for Energy Research
Schweizerische Eidgenossenschaft
Confédération suisse
Confederazione Svizzera
Confederaziun svizra
Swiss Confederation
Commission for Technology and Innovation CTI

Numerical Modeling of Natural Convection in Fractured Media

James Patterson, Thomas Driesner
Institute of Geochemistry and Petrology, ETH Zurich, Switzerland

Before EGS: In-situ Geothermal Gradient

Geothermal gradient is a key reservoir characteristic in determining how deep a well must be drilled to reach a certain temperature. However, faults and fractures in these rocks may facilitate natural convection: the process by which thermally-induced density differences of water cause cold, dense water to cycle deeper into the basement while hot, light water moves towards the surface. This can result in spatially varying temperatures around the upward/downward flowing plumes and can dramatically influence produced fluid temperature. This research seeks to better understand the role of natural convection in fractures on temperature variations in the subsurface and its implications for geothermal energy. We use the Complex Systems Modeling Platform (CSMP++), a reservoir modeling platform developed in part at ETH Zurich.

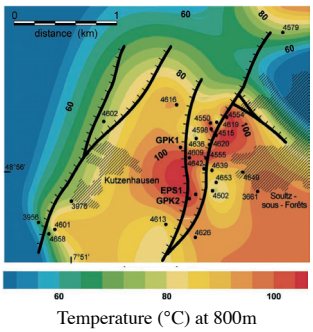

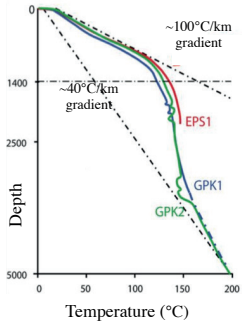

Fig. 1 (left): *Measured and interpolated temperature at 800m depth; irregular shape distribution indicates convective plumes.*[1]
Fig. 2 (right): *Temperature profile to 5000m depth in 3 wells featured in Fig. 1. Sharp drop in gradient around 1400m due to impermeable layer blocking convection.*[2]

Thermal Perturbation from Convection in a Single Fracture

As fluid at the bottom of a fracture is heated, it rises through the highly permeable fracture, carrying heat to the top of up-flow zones, while cold fluid sinks and cools the rock at the bottom of down-flow zones. The spacing and strength of these up- and down-flow zones are primarily a function of fracture aperture/permeability. Complex 3-dimensional thermal perturbations form around the fracture. Heating patterns above the fracture may be indicative of individual, wide convection cells or multiple narrow cells along a fracture in the subsurface.

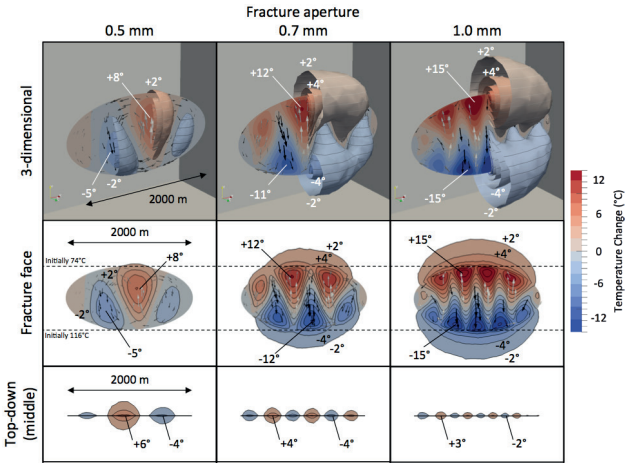

Fig. 3: *Change in temperature around a fracture with aperture 0.5 mm, 0.7 mm, and 1.0 mm. Larger apertures result in narrower convection cells and stronger heating/cooling of host rock.*

References

[1] Clauser, C., Griesshaber, E., Neugebauer, H.J. (2002) Decoupled thermal and mantle helium anomalies: Implications for the transport regime in continental rift zones. Journal of Geophysical Research, Vol. 107.
[2] Siffert, D., Haffen, S., Garcia, M.H., Geraud, Y. (2013) Phenomenological study of temperature gradient anomalies in the Buntsandstein formation, above the Soultz geothermal reservoir, using TOUGH2 simulations. 38th Stanford Workshop on Geothermal Reservoir Engineering.

Flow Patterns Around a Single Fracture

Convection within a fracture also induces fluid flow in permeable host rocks. Two forces drive fluid flow around the fracture:

- Circulation of fluid in the fracture drives fluid inflow/outflow through the fracture walls
- The convection-driven thermal perturbation heats/cools fluid near the fracture, inducing buoyancy-driven fluid flow in the host

The combination of inflow/outflow (flow perpendicular to fracture face) and buoyant forces (vertical flow) creates secondary convection cells that circulate parallel to fracture strike (in the 0.7 and 1.0 mm cases).

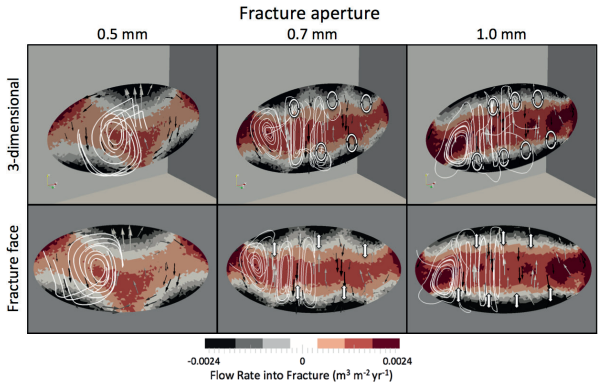

Fig. 4: *Inflow (red) and outflow (black) patterns in a fracture with 0.5 mm, 0.7 mm, and 1.0 mm aperture. Fluid flow streamlines show complex patterns surrounding fracture, including secondary convection cells forming in the 0.7 and 1.0 mm cases.*

Multiple Heterogeneous Fractures

Real fractures have heterogeneous aperture distributions, creating regions of high or low permeability. This influences the location and strength of natural convection cells. Additionally, fractures typically occur in sets of multiple fractures with similar orientations. The thermal perturbation caused by natural convection affects convection patterns in neighboring fractures, creating a "synchronization" effect – up-flow and down-flow regions will self-organize and create convection "rolls" across multiple fractures.

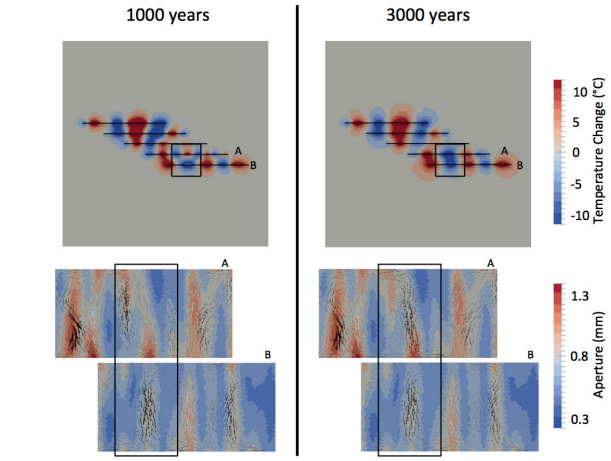

Fig. 5: *Bird's-eye view of slice at 2500 m depth; two intersecting fracture sets. Colored by temperature difference. Convection tubes form across fractures, regardless of fracture length.*

Conclusions and Future Work

Fundamental understanding of thermal perturbations created by convection within a fracture aids us in understanding subsurface fracture and flow networks. Additionally, further insight may be gained by accounting for more complicated physical processes (e.g. thermo-mechanics), modeling site-specific geometries, and by investigating optimal well placement in such a setting.

SCCER SoE
SWISS COMPETENCE CENTER for ENERGY RESEARCH
SUPPLY of ELECTRICITY

SCCER-SoE Annual Conference 2017

In cooperation with the CTI
Energy
Swiss Competence Centers for Energy Research
Schweizerische Eidgenossenschaft
Confédération suisse
Confederazione Svizzera
Confederaziun svizra
Swiss Confederation
Commission for Technology and Innovation CTI

Enhancing drilling performance by combining conventional and thermal spallation drilling: A feasibility study

Edoardo Rossi[a,b], Michael A. Kant[b], Claudio Madonna[a], Martin O. Saar[a], Philipp Rudolf von Rohr[b]

[a]ETH Zürich, Department of Earth Sciences, Sonneggstrasse 5, 8092 Zürich
[b]ETH Zürich, Institute of Process Engineering, Sonneggstrasse 3, 8092 Zürich

Motivation

The utilization of deep geothermal energy is impeded by the high drilling costs, which account for more than 40% of the total investment for a geothermal power plant [1]. Currently employed drilling methods are based on mechanical abrasion and exportation of the rock, resulting in substantial drill bit wearing and low rates of penetration (ROP) in hard rocks.
A novel approach is to implement a thermal assistance at the front face of the drill bit to enhance the performance of conventional rotary drilling and reduce the overall costs.

Concept

A hot-jet is used to thermally assist the conventional drilling by inducing shock heating and therefore thermally weakening the rock material. The material exportation would therewith require lower forces on the drill bits which also implies reduced drill bit wearing.

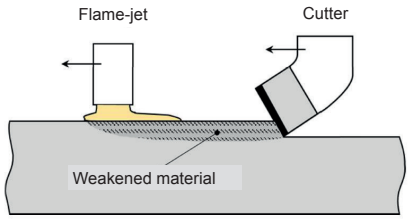

Figure 1: Concept of combined thermo-mechanical drilling [2]

Combined thermo-mechanical drilling

The combined drill head features:

- Fuel (methane) and oxidizer (air) used as reaction fluids
- A combustion chamber where the fluids are combusted
- The drilling mud is also used to cool down the combustion chamber
- At the bit face a flame slot is prescribed
- Conventional cutters are placed next to flame-jets

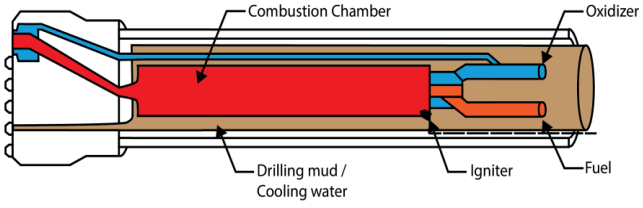

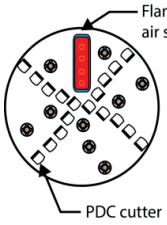

Flame nozzles include an ***air-shielding*** concept:

- Constrain and maximize flame heat transfer to the rock
- Guarantee low temperatures at the cutters

Figure 2: Potential implementation of combined thermo-mechanical method [3]

Preliminary experiments

In order to evaluate the weakening effects of high heating rates-flame treatments, the strength after heating of Rorschach sandstone and Central Aare granite are analyzed. Different heating rates are studied to highlight the different behavior of the rocks after oven and flame heating.

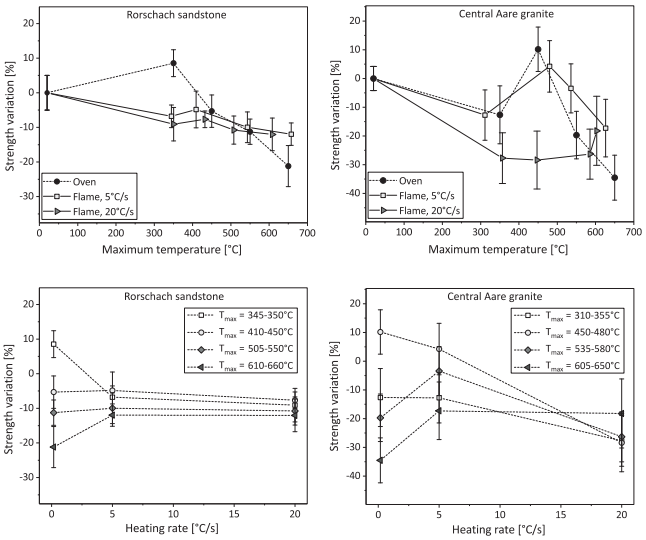

Figure 3: Rock strength variation for different treatment temperatures and heating rates

→ No hardening behavior after flame heating for sandstone and granite
→ Sandstone material is weakened for any temperature when flame-treated
→ 30% strength decrease of granite when treated at high heating rates
→ Low heating rates: thermal cracking due to thermal expansion stresses
→ High heating rates: thermal cracking due to high thermal gradients

Conclusions

The feasibility of the combined drilling method was demonstrated by means of the strength reduction after treating the rock with a flame-jet. Thus, local and high heating rate flame treatments can be implemented to weaken the rock material yielding lower forces on the drill bits and therefore increased performance and reduced drilling costs.

Additionally, the shielding of the flame is fundamental to allow this method to be effectively applicable and to be used in the field as an alternative drilling approach.

As a final step, the technology shall be implemented in order to finally prove the applicability and the related improvements in terms of drilling performances.

References

[1] Tester J.W. et al. (2006). The future of geothermal energy: Impact of enhanced geothermal systems (EGS) on the United States in the 21st century, *Massachusetts Institute of Technology*

[2] Rossi E. et al. (2017). The effects of flame-heating on rock strength: Towards a new drilling technology. *51st US Rock Mechanics/Geomechanics Symposium 25-28 June 2017, San Francisco, USA.*

[3] Kant M.A. et al. (2017) Enhancing the drilling process for geothermal resources by combining conventional drilling and the spallation technology. *Proceedings, 42nd Workshop on Geothermal Reservoir Engineering, Stanford: Stanford University, 2017*

IPE Institute of Process Engineering
DERDW EARTH SCIENCES
GEO
Schweizerische Eidgenossenschaft
Confédération suisse
Confederazione Svizzera
Confederaziun svizra
Bundesamt für Energie BFE
Swiss Federal Office of Energy SFOE
GZB INTERNATIONALES GEOTHERMIEZENTRUM
INTERNATIONAL GEOTHERMAL CENTRE

SCCER-SoE Annual Conference 2017

Pico-seismicity during hydraulic stimulation experiments at the Grimsel Test Site

Linus Villiger*, Valentin Gischig**, Joseph Doetsch**, Hannes Krietsch**, Mohammadreza Jalali**, Nathan Dutler ***, Benoît Valley ***, Keith Evans**, Florian Amann** & Stefan Wiemer*

* Swiss Seismological Service, ETH Zurich, CH-8092 Zurich; ** Department of Earth Sciences, ETH Zurich, CH-8092 Zurich;
***Centre for Hydrogeology and Geothermics, University of Neuchâtel, CH-2000 Neuchâtel

Introduction

The In-situ Stimulation and Circulation (ISC) experiment at the Grimsel Test Site (GTS) is an ongoing interdisciplinary project to study the pressure, temperature and stress changes in the rock mass due to hydraulic stimulation (Amann et al., 2017; Gischig et al., 2017). In early 2017, the project entered the second phase, which included the main stimulation experiments. It involved high-pressure fluid injections into two shear zones (S1, S3) along which slip was induced (i.e. hydraulic-shearing). In May 2017 the second series of experiments followed. These experiments involved injection at even higher pressures and larger flow rates which induced tensile-dominant fracturing (i.e. hydraulic fracturing). The entire experiment series was established to support research related to deep geothermal energy which should play a significant role in the Swiss energy mix by 2050 (Swiss Energy Strategy 2050).
Six sections (HS02, 04, 05, 03, 08, 01) of 1 to 2 m length distributed over the two injection boreholes were stimulated during the hydraulic shearing experiments (HS). Six different sections in intact rock within the same boreholes were stimulated during the hydraulic fracturing experiments (HF). During the experiments a multi-sensor monitoring system was in place:

Hydraulic monitoring
- injection pressure, flow rate
- pressure monitoring boreholes

Deformation monitoring
- fiber-optics (FBG's, distributed) in deformation monitoring boreholes
- 3 tilt meters in VE tunnel
- 4 extensometers in AU tunnel

Seismic monitoring
- continuous acquisition at 200 kHz
- 26 Acoustic emission sensors in tunnels and seismic monitoring boreholes
- 5 accelerometer in tunnels
- 2 seismic sources in boreholes, 8 hammers in tunnels

Seismic monitoring network at GTS

The figure below shows an overview of the seismic monitoring network installed during the performed experiments at GTS. The intervals stimulated during experiment HS01 and HS04 are highlighted in red.

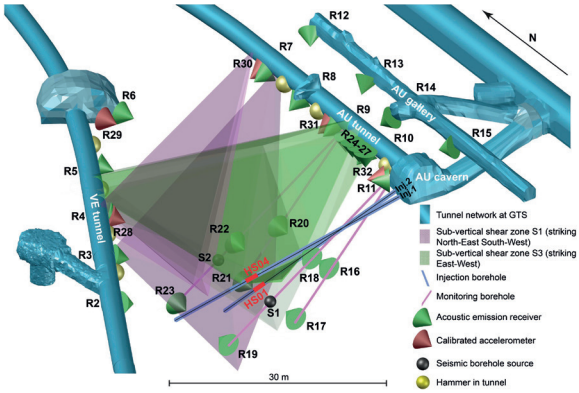

Overview hydraulic-shearing experiments

Only the HS experiments are considered in this poster. In the following, injectivity increase of all HS experiments estimated from the slope of injection pressure vs. flow rate at low pressure during step-pressure tests are stated. Experiments show a high variety in seismic response as well as in injectivity gain even though the injection protocol as well as the amount of injected volume was similar for all experiments. The stimulation of shear zone S3 generates a much higher seismic response compared to injections into shear zone S1.

Experiment	Injection in, interval *[m]*	Structure	Initial injectivity, final injectivity *[l/min/MPa]*	Change in injectivity *[ ]*	Inj. Volume *[liter]*	Total events *[ ]*
HS02	Inj1, 38.0 - 40.0	S1	0.018, 1.62	89	797	1203
HS04	Inj1, 27.2 - 28.2	S3	0.9, 0.9	1	1253	5606
HS05	Inj1, 31.5 -32.5	S3	0.086, 0.4	5	1211	2452
HS03	Inj1, 34.3 - 35.3	S1	0.0035, 1.7	486	831	314
HS08	Inj1, 22.0 - 23.0	S1 (S3)	0.002, 0.54	270	1258	3703
HS01	Inj2, 39.8 - 40.8	S1	0.0006, 1.11	1850	982	560

Event evolution during hydraulic shearing experiments

This section shows, flow rate, injection pressure and cumulative number of seismic events for experiment HS01 and HS04. During HS01 shear zone S1 and during HS04 shear zone S3 was stimulated. Events which are detected at all 8 borehole stations (R16 - R23) and more stations in the surrounding tunnels contribute to the cumulative number of events of coinc. 8. Events which are detected at 7 borehole stations and other surrounding stations contribute to coinc. 7 and so forth. The vertical stripes on top of the "cumulative number of events" line indicate performed seismic surveys during which the search for induced seismic events was suspended.
All experiments show, after breakdown of the respective interval, a threshold pressure which has to be reached to initiate seismicity. Some seismic events are initiated after shut-in. Also the subsequent venting phase initiates seismic events.

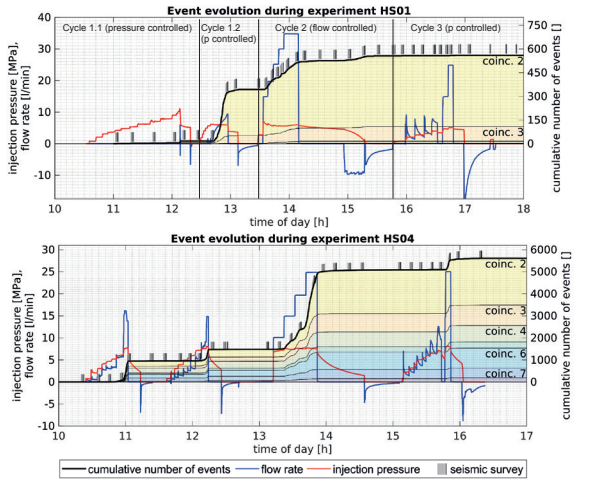

Location of seismicity during experiment HS04

The figure below shows the absolute location of 1000 events of experiment HS04 in a view towards North (A), a view towards West (B) and in top view (C). The highest accuracy in location is thereby achieved by locating the events of coincidence level 8. The error in location increases with decreasing coincidence level (i.e. with decreasing detection quality). The location of the presented events was performed using manually picked P-wave arrivals in a homogeneous and isotropic velocity model having a P-wave velocity of 5150 m/s. The relative magnitude (Mr) stated was determined from recorded peak amplitudes of the respective event.

Already, the location using this simple velocity model shows a clustering of events, as well as a clustering of high magnitude events.

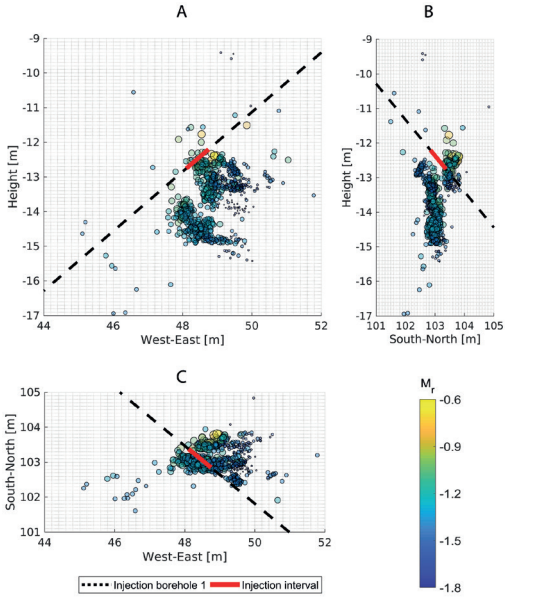

Conclusion and Outlook

- The performed hydraulic-shearing experiments show high variability in injectivity gain as well as in seismic response. Exceeding a specific injection pressure onsets seismicity. Induced seismic events tend to form cluster in both spatial distribution and magnitude.
- In a next step, event location will be performed for all 12 experiments with more advanced location techniques (e.g. joint hypocenter determination), additionally location accuracy will be quantified.

Reference

- Amann, F., et al. (2017), The seismo-hydro-mechanical behaviour during deep geothermal reservoir stimulation: open questions tackled in a decameter-scale in-situ stimulation experiment. Solid Earth Discuss., https://doi.org/10.5194/se-2017-79
- Gischig, V.S., Doetsch, J., Maurer, H., Krietsch H., Amann F., Evans, K.F., Nejati, M., Jalali, M., Valley, B., Obermann, A., Wiemer, S. and Giardini, D. (2017), On the link between stress field and small-scale hydraulic fracture growth in anisotropic rock derived from microseismicity. Solid Earth Discuss., https://doi.org/10.5194/se-2017-78

Email: linus.villiger@sed.ethz.ch

SCCER SoE
SWISS COMPETENCE CENTER for ENERGY RESEARCH
SUPPLY of ELECTRICITY

SCCER-SoE Annual Conference 2017

In cooperation with the CTI
Energy
Swiss Competence Centers for Energy Research
Schweizerische Eidgenossenschaft
Confédération suisse
Confederazione Svizzera
Confederaziun svizra
Swiss Confederation
Commission for Technology and Innovation CTI

An Implicit Level Set Scheme to simulate planar 3D hydraulic fracture propagation

GeoEnergyLab

Haseeb Zia, Brice Lecampion

FNSNF
Swiss National Science Foundation

Motivation

Hydraulic fractures are tensile fractures that propagate in an initially stressed rock due to the injection of fluid at a given rate. Simulating the propagation of such fractures is a challenge as there are multiple processes involved that are operating at multiple scales. Numerically capturing these processes on the full range of both temporal and spatial scales is challenging and has been the subject of many studies in the last few decades. The Implicit Level Set Algorithm (ILSA) [Peirce & Detournay 2008] is one such numerical scheme that aims at resolving these multiscale processes with relatively low computational cost. We present here an open-source Python implementation of this scheme.

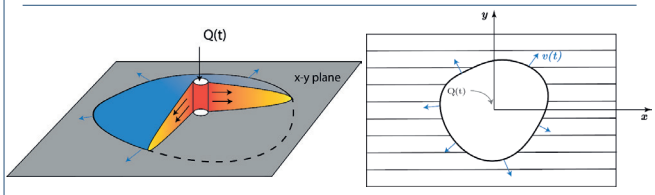

Fig 1: The fracture is assumed to be planar (propagating in x-y plane)

ILSA Scheme

The Implicit Level Set Algorithm (ILSA) simulates the propagation of planar 3-dimensional hydraulic fractures. The solution of elasticity and the fluid flow is obtained in a fully coupled manner. The propagation is tackled combining a level set scheme and the hydraulic fracture tip solution [Garagash et al. 2011]. The following numerical techniques are used to solve the coupled problem.

- Finite Volume method for the fluid flow.
- Displacement discontinuity method for elasticity.
- Level set method to track the fracture front.

The scheme uses a Cartesian grid. The main strength of the scheme is its utilization of the plane-strain semi-infinite hydraulic fracture solutions to capture the near-tip behaviour. This allows it to compute the solution on a relatively coarse grid, making it both accurate and computationally efficient.

Governing Equations

The following equations describe the process of hydraulic fracture propagation.

- Elasticity for planar mode I fracture can be re-written as the following boundary integral equation

$$p = p_f - \sigma = -\frac{E'}{8\pi}\int_{A(t)} \frac{w(x',y',t)dA(x',y')}{[(x'-x)^2+(y'-y)^2]^{3/2}}$$

[Hills et al. 1996]

- Fluid continuity:

$$\frac{\partial w}{\partial t} + \nabla \cdot q + g_L = Q(x,y)\delta(x,y),$$

with Poiseuille law and Carter leak-off:

$$q = -\frac{w^3}{\mu'}\nabla p_f, \quad g_L = \frac{C'H(t-t_0(x,y))}{\sqrt{t-t_0(x,y)}}$$

Tip Asymptotics

It can be shown that the equations governing the near tip behaviour of the fracture are identical to the governing equations for the problem of a steadily propagating semi-infinite fluid driven fracture [Desroches et al. 1994, Garagash & Detournay 2000, Garagash et al. 2011]. In the near-tip region, these equations provide the exact relations between the fracture parameters such as width and pressure, and the distance from the front.

For example, in the limiting toughness (Eq. a) and viscosity (Eq. b) dominated cases, the fracture width in the tip region is given by

$$\hat{w} = \frac{K'}{E'}\hat{x}^{1/2} \quad \text{(a)} \qquad \hat{w} = (18\sqrt{3}V\frac{\mu'}{E'})^{1/3}\hat{x}^{2/3} \quad \text{(b)}$$

[J.R. Rice 1968] [Garagash et al. 2000].

The complete solution capturing the transition between different propagation regimes has been obtained numerically [Garagash et al. JFM 2011]. Here, we are using the approximation provided by Dontsov and Peirce [2015]. The ILSA scheme couples these tip solutions with the finite fracture discretization to resolve the tip behaviour at the sub-grid scale.

Validation

The scheme has been validated with a number of test cases. The figures below show the comparison of the solution computed by the ILSA scheme against the analytical solution for the case of viscosity dominated propagation.

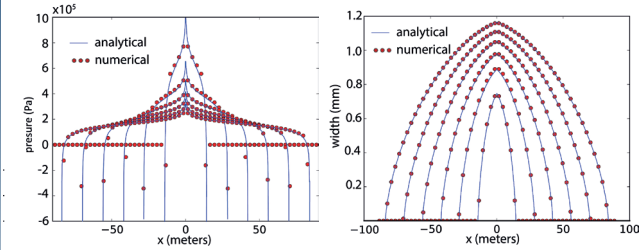

Fig 2: Time evolution of fracture width and pressure at the x-axis line.

Further test cases

- Confined propagation

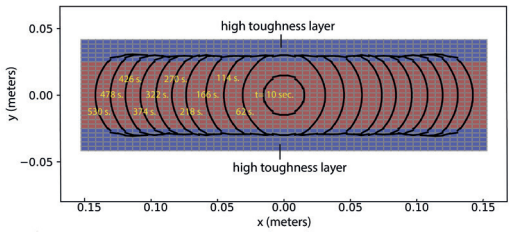

Fig 3: Footprint of a fracture propagating in a layer confined by high toughness layers

- Asymmetric Stress contrast

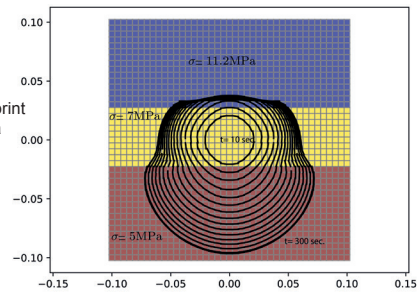

Fig 4: Time evolution of footprint of a fracture propagating in a layer bounded by layers with different confining stresses.

References

- Peirce, A., & Detournay, E. (2008). An implicit level set method for modeling hydraulically driven fractures. Computer Methods in Applied Mechanics and Engineering, 197(33), 2858-2885.
- Hills, D. A., Kelly, P. A., Dai, D. N., & Korsunsky, A. M. (2013). Solution of crack problems: the distributed dislocation technique (Vol. 44). Springer Science & Business Media.
- Rice, J. R. (1968). Mathematical analysis in the mechanics of fracture. Fracture: an advanced treatise, 2, 191-311.
- Garagash, D., & Detournay, E. (2000). The tip region of a fluid-driven fracture in an elastic medium. Transactions-American Society of Mechanical Engineers, Journal of Applied Mechanics, 67(1), 183-192.
- Desroches, J., et al. "The crack tip region in hydraulic fracturing." Proceedings of the Royal Society of London A: Mathematical, Physical and Engineering Sciences. Vol. 447. No. 1929. The Royal Society, 1994.
- Garagash, D. I., Detournay, E., & Adachi, J. I. (2011). Multiscale tip asymptotics in hydraulic fracture with leak-off. Journal of Fluid Mechanics, 669, 260-297.